Scientific Reports

https://doi.org/10.1038/s41598-026-52765-4

Article in Press

Petrogenesis and geodynamics of the Early Miocene Kashan granitoids in the central Urumieh-Dokhtar Magmatic Arc, Iran

Received: 30 March 2026

Accepted: 7 May 2026

Published online: 11 May 2026

Cite this article as: Kou C., Zhang H. & Zhu M. Petrogenesis and geodynamics of the Early Miocene Kashan granitoids in the central Urumieh-Dokhtar Magmatic Arc, Iran. *Sci Rep* (2026). https://doi.org/10.1038/s41598-026-52765-4

Caihua Kou, Hongrui Zhang & Mingyu Zhu

Petrogenesis and geodynamics of the Early Miocene Kashan granitoids in the central Urumieh-Dokhtar Magmatic Arc, Iran

Caihua Kou[1], Hongrui Zhang[1*], Mingyu Zhu[1]

1. State Key Laboratory of Deep Earth and Mineral Exploration, Institute of Geology, Chinese Academy of Geological Sciences, Beijing, 100037, China

** Corresponding author: zhanghr@yeah.net*

This study investigates the early Miocene granitoids (rhyolites, dacites, granodiorites, and diorites) from the Kashan area in the central Urumieh-Dokhtar Magmatic Arc of Iran, to constrain their sources and geodynamic processes. Zircon U–Pb ages, zircon Hf isotopic data, and whole-rock geochemistry are presented. The diorites yielded a zircon U–Pb age of 22 Ma. They are geochemically classified as non-adakitic rocks, characterized by low Sr (258.0–289.5 ppm) and high Y (28.21–29.33 ppm) with low Sr/Y (9.04–9.92). These rocks exhibit high-K calc-alkaline affinities, enrichment in light rare earth elements (LREEs), pronounced negative Nb–Ta anomalies, high initial $^{87}Sr/^{86}Sr$ ratios (0.706181–0.706269), coupled with negative εNd(t) (−3.6 to −3.0) and εHf(t) (−3.5 to −0.9) values. These features indicate that the diorites were derived from partial melting of an enriched subcontinental lithospheric mantle (the amphibole-bearing spinel stability field) metasomatized by subducted sediment-derived fluids. In contrast, the rhyolites, dacites, and granodiorites exhibit adakitic affinities, showing high Sr (377.2–595.4 ppm), low Y (4.36–13.48 ppm) with high Sr/Y (29.93–94.28). They display high SiO_2 (63.01–77.33 wt%) and low MgO (0.74−2.45 wt%),

Mg# (29–47), and Ni (4.56−22.13) values. Such signatures are consistent with partial melting of the thickened lower crust. Based on the regional geology and previous work, we propose a two-stage geodynamic model. The diorites formed during the initial Arabia-Eurasia collision related to the final breakoff of the Neo-Tethys slab, whereas the adakitic rocks were generated during the main collisional stage.

Keywords the Early Miocene granitoids; Geochronology; Petrogenesis; Geodynamic processes; the central UDMA in Iran

The Neo-Tethyan tectonic domain records a dynamic geological history, characterized by the opening and closing of the Neo-Tethys Ocean and subsequent continental collision between Arabia and Eurasia, which resulted in the formation of the NW-SE trending Zagros Orogen belt in Iran[1–8]. The Zagros Orogen belt comprises the following major units from southwest to northeast: the Zagros Fold-and-Thrust Belt (ZFTB), the Sanandaj-Sirjan Magmatic-Metamorphic Zone (SSZ), and the Urumieh-Dokhtar Magmatic Arc (UDMA)[9–12]. Among them, the UDMA fully captures the magmatic and tectonic responses during the transition from oceanic subduction to continental collision. Therefore, it constitutes an outstanding natural geological laboratory for investigating magma genesis and deep geodynamic processes. Currently, considerable research has investigated the Cenozoic igneous activity in the UDMA[13–26]. However, there is still no consensus on the geodynamic processes driving the early Miocene magmatism in the UDMA. Key points of contention include whether it resulted from subduction-related

processes preceding the initial continental collision of Arabia-Eurasia at ca. 25–23 Ma[11, 14, 23–24, 27–31] or from post-collisional extension following the continental collision at ca. 37–23 Ma[32–41]. Unfortunately, crucial evidence to support these models is not sufficient.

The Early Miocene records not only a key shift from pre- to post-collisional magmatism, but also a fundamental transition of the regional tectonic regime and deep geodynamic evolution. Magmatism from this period provides critical insights into the evolution of the Arabia-Eurasia continental collision, as well as the interactions among the subducted slab, lithospheric mantle, asthenosphere, and continental crust. Our recent investigations in the Kashan area, located in the central UDMA, Iran, have identified an Early Miocene diorite and adakitic rocks (rhyolite, dacite, and granodiorite). We present integrated U–Pb zircon geochronology, Lu–Hf isotopes, whole-rock major and trace elements, and Sr–Nd isotopic compositions of these rocks. Based on these new results, we evaluate their petrogenesis and crust-mantle interaction, and provide new insights into the associated deep geodynamic processes.

Geological Setting

The NW-SE trending Urumieh-Dokhtar Magmatic Arc (UDMA) is a fundamental component of the Zagros Orogen belt, extending approximately 2000 km in length and 50 to 80 km in width. It lies parallel to the Zagros Fold–Thrust Belt (ZFTB) and the Sanandaj-Sirjan Zone (SSZ) to the southwest (Fig. 1a). The oldest exposed stratigraphic units within the UDMA consist of

Paleozoic to Mesozoic sedimentary rocks, including limestone, dolomite, sandstones, and shales, which show no evidence of metamorphism[1]. The outcropped strata in the UDMA range from Paleozoic through Mesozoic to Cenozoic sequences (Fig. 1b). The UDMA represents a key province of Cenozoic magmatic activity in Iran, comprising thick (~4 km) sequences of extrusive and intrusive rocks, along with associated volcanoclastic units[14, 20–21, 27]. A significant magmatic flare-up occurred during the Eocene and Oligocene, marked by the emplacement of calc-alkaline magmas[1, 14, 20, 27, 42–43] (ca. 55–35 Ma). From the Late Oligocene to Miocene (ca. 30–5 Ma), magmatism continued with the emplacement of calc-alkaline suites, which also exhibit ultrapotassic and adakitic affinities[14, 24, 27–29, 31, 33, 36, 39–41, 44–52] (Fig. 1a). Subsequent magmatic activity during the Pliocene–Quaternary produced scattered alkaline rock series with intraplate-like geochemical signatures[39, 53–54].

The Miocene igneous rocks in central UDMA and Sampling

The Miocene igneous rocks in central UDMA

Numerous Miocene igneous rocks, formed during the early to late Miocene (ca. 24–5 Ma), are exposed in the Qom, Kashan, Natanz, Nain, and Yaza areas[13, 24, 28–29, 31, 40, 48, 50, 52] (Fig. 1a). These rocks consist of basalt, gabbro, basaltic andesite, andesite, diorite, dacite, rhyolite, granodiorite, and granite. Among them, most early Miocene rocks are non-adakitic rocks and belong to calc-alkaline and high-K calc-alkaline magmatic series[13, 24, 28–29, 31, 40, 48, 50, 52], whereas minor early Miocene intermediate–felsic rocks (18.67 Ma) exhibit

adakitic characteristics and are affiliated with calc-alkaline magmatic series[28–29]. In addition, certain late Miocene intermediate rocks display alkaline affinities and are classified as shoshonite[24]. As a whole, the Miocene rocks show subduction-related geochemical signatures, characterized by depletions in Nb, Ta, and Ti. Some authors attributed this subduction-related affinity to subduction processes during the final stage of subduction, which lasted until the early Miocene[11, 14, 27, 24, 55]. Other researchers, however, suggest that these rocks were derived from either asthenospheric mantle or lithospheric mantle that had been metasomatized by subduction-related materials within an extensional setting triggered by slab rollback and/or breakoff[11, 28–29]. The early Miocene adakitic rocks are interpreted to have formed by decompression-induced partial melting of the slab[28]. The late Miocene shoshonite formed in a post-collisional setting[24].

Samples in this study

The study areas are regarded as the central UDMA (Fig. 1a, b), which refers to the Qom, Kashan, Natanz, and Nain regions. The reported ages for Miocene granitoids in the central UDMA suggest that magmatism was episodic, predominantly occurring between 24 and 15 Ma[23, 27, 50]. Among these granitoids, both non-adakitic and adakitic affinities have been recognized[13, 27, 29, 32, 38]. The sampling locations are situated in the southern Kashan area, within the central UDMA (Fig. 1a, b). Samples were systematically collected from Miocene granitoids, including diorite, granodiorite, dacite, and rhyolite (Fig. 1b; Supplementary Table 1).

Rhyolites are moderately porphyritic, containing 5–10% phenocrysts of euhedral to subhedral plagioclase, sanidine, and minor biotite and quartz (Fig. 2a, b). The plagioclase phenocrysts are tabular, ranging from 0.2 to 2 mm in size, and exhibit well-developed polysynthetic twinning and oscillatory zoning. Quartz and sanidine phenocrysts, the latter displaying carlsbad twining, are typically 0.5 to 1 mm in size. Ferromagnesian minerals are scarce, represented by a few yellow to brown, euhedral biotite grains, 1–2 mm in size. The groundmass is generally microcrystalline and consists of the same mineral phases observed as phenocrysts, along with Fe-Ti oxide.

Dacites display a weakly to moderately porphyritic texture with less than 15% phenocrysts (Fig. 2c, d). The phenocryst assemblage is dominated by plagioclase and K-feldspar with minor clinopyroxene. The plagioclase plates are mostly euhedral to subhedral and tabular in shape, ranging from 0.2 to 2.5 mm in size. The K-feldspar grains are mostly euhedral to subhedral up to 2.0 mm in size. The clinopyroxene is less common, typically fresh, and occurs as euhedral to subhedral grains ranging from 0.5 to 2.0 mm in size. The groundmass is generally microcrystalline and consists of the same phases observed as phenocrysts with sparse accessory opaque minerals (such as Fe-Ti oxide).

Granodiorites contain variable proportions of medium- to coarse-grained, euhedral to subhedral minerals (Fig. 2e, f). The main phases include plagioclase (60–70 vol%; 0.5–2.0 mm), K-feldspar (5–10 vol%; 0.5 mm), biotite (5–10 vol%; 0.5–2.5 mm), and hornblende (5–10 vol%; 2.0 mm). Quartz (15–

20 vol%) mainly occurs as fine-grained or microcrystalline aggregates filling the interstices between other grains (Fig. 2e, f). Many plagioclase crystals exhibit well-developed polysynthetic twinning and oscillatory zoning (Fig. 2e, f). The primary accessory minerals are Fe-Ti oxides, titanite, zircon, and apatite.

Diorites are dominated by variable proportions of plagioclase (70–80 vol%) and hornblende (10–20 vol%), along with minor Fe-Ti oxides, titanite, and apatite (Fig. 2g, h). The plagioclase crystals are mainly tabular and euhedral to subhedral in shape, with grain sizes varying from 0.5 to 3.0 mm. They generally exhibit well-developed polysynthetic twinning. The hornblende grains occur as euhedral to subhedral grains, ranging from 0.5 to 1.5 mm.

Analytical methods

One diorite sample (NA12–38–6) was selected for zircon separation and U–Pb dating. Zircon grains were extracted using conventional heavy liquids and magnetic techniques, and then purified by hand-picking under a binocular microscope. Representative zircon grains were mounted in epoxy resin and polished down to expose the grain centre. Internal structures of the zircon grains were examined using transmitted electron, backscattered electron (BSE), and cathode luminescence (CL) before analysis, to investigate their morphology and internal structures. The zircon U–Pb isotopic analyses were carried out on an Elan 6100 DRCII quadrupole–inductively coupled plasma–mass spectrometer (Q-ICP-MS) coupled to a GeoLas Pro 193 nm ArF excimer laser-ablation system at the University of Science and Technology of China,

Hefei, China. A beam of 32 μm in diameter was used. The analytical and data reduction procedures follow those described by Yuan et al.[56]. A 91500 standard zircon was used for internal standardization during U–Pb dating, whereas NIST 610 and 612 reference materials were monitored as external standards. Data were processed using the GLITTER and ISOPLOT[57] programs.

In situ zircon Lu–Hf isotopic analysis was carried out with a Neptune multi-collector ICP-MS (Thermo-Finnigan) equipped with a Geolas-193 laser-ablation system at the Institute of Geology and Geophysics, Chinese Academy of Sciences (Beijing). The analytical spots were made at U–Pb dating spots, with a beam diameter of 32 μm and an 8 Hz repetition rate. A weighted mean $^{176}Hf/^{177}Hf$ value of the reference standard GJ1 is 0.282015 ± 8 (2σ, n = 10), which is consistent within error[58] (0.282015 ± 19) and with that obtained in the laboratory (0.282008 ± 20). Instrumental conditions, analytical procedures, and data acquisition were reported in detail in Hou et al.[59].

The samples were crushed and powdered to 200 mesh in an agate mill for compositional analysis. Whole rock geochemical data were obtained at Guangzhou Institute of Geochemistry, Chinese Academy of Sciences (GIGCAS). Major element oxides were analyzed by a Rigaku ZSX100e X-ray fluorescence spectrometer (XRF). Loss on ignition was determined gravimetrically after heating the samples at 1000°C for 1 hour. The analytical uncertainties are generally less than 2%. Trace element concentrations were determined using an inductively coupled plasma-mass spectrometer (ICP-MS)

using the analytical procedures described by Chen et al.[60]. The analytical uncertainties are less than 5%.

The Sr–Nd isotopes were analyzed using a Finnigan MAT Triton TI TIMS at CAS Key Laboratory of Crust-Mantle Materials and Environments, School of Earth and Space Sciences, University of Science and Technology of China (USTC), Hefei, China[60]. Sr isotopic data were normalized to $^{86}Sr/^{88}Sr$ = 0.1194, and the NBS-987 Sr standard yielded an average value of 0.710244 ± 0.000033 (2σ). Nd isotopic data were normalized to $^{146}Nd/^{144}Nd$ = 0.7219, and the JMC Nd_2O_3 standard yielded an average value of 0.511149 ± 0.000022 (2σ).

Results

U–Pb zircon age

The results of zircon U–Pb analyses are listed in Table 1. The zircon grains separated from the diorites (sample NA12–38–6) exhibit transparent, euhedral, and prismatic morphologies (50–100 μm in length, 1:1–2:1 aspect ratios) with homogeneous cathodoluminescence (CL) textures lacking obvious oscillatory zoning (Fig. 3a). The relatively high Th/U values of 0.35–0.86 supported an igneous origin[61]. Eleven analyzed grains yielded a dispersed age spectrum of 26.6–34.4 Ma (Fig. 3b). Ten analytical spots yield a concordia age of 22.1 ± 0.1 Ma (Fig. 3c) with a similar weighted mean $^{206}Pb/^{238}U$ age of 22.1 ± 0.5 Ma (Fig. 3d), indicating that the crystallization age of the diorite is 22 Ma. In addition, rocks with adakitic affinities formed in the Qom and Kashan areas of the central UDMA at 17–19 Ma[27]. Based on

this, we consider the adakitic rocks in our study from the Kashan areas, namely, the granodiorite, dacite, and rhyolite (see below), to have an emplacement age of 17 Ma.

Whole-rock major and trace element compositions

The whole-rock major (all normalized to 100% anhydrous) and trace element compositions are presented in Table 2. The rhyolites have the highest SiO_2 (69.76–70.33 wt%), moderate MgO (0.74–0.84 wt%), and relatively low total alkalis ($Na_2O + K_2O$ = 6.87–7.01 wt%), K_2O (2.55–2.63 wt%), and FeO^T (2.52–3.00 wt%) contents. They plot in the sub-alkaline series field on the SiO_2 versus K_2O+Na_2O diagram (Fig. 4a) and in the calc-alkaline field on the SiO_2 versus K_2O diagram (Fig. 4b). They are peraluminous with high A/CNK ratios (molecular ratio of $Al_2O_3/(CaO + Na_2O + K_2O)$) ranging from 1.45 to 1.54 (Fig. 4c). They exhibit low K_2O/Na_2O ratios (0.59–0.61) (Fig. 4d) and $Mg^{\#}$ values ($100 \times Mg/[Mg + Fe^{2+}]$ = 32.7–39.8). On the Chondrite-normalized rare earth element (REE) patterns (Fig. 5a), the rhyolites exhibit extremely fractionated light rare earth elements (LREEs) relative to medium rare earth elements (MREEs) and heavy rare earth elements (HREEs) as reflected in high $(La/Sm)_N$ (6.44–6.56) and $(La/Yb)_N$ (47.97–51.21; subscript N: chondrite-normalized) ratios. The samples lack significant Eu anomalies with Eu/Eu* ($2\times Eu_N/(Sm_N+Gd_N)$) values of 0.88–0.91 (Fig. 5a). On the primitive mantle normalized trace element spider diagram (Fig. 5b), they are strongly enriched in large ion lithophile elements (LILEs; e.g., Th and U) and significantly depleted in heavy field strength elements (HFSEs; e.g., Nb, Ta,

and Ti). Notably, the rhyolites exhibit geochemical affinities to adakitic rocks, characterized by high Sr (408.9–416.7 ppm), low Y (4.36–4.47 ppm) and Yb (0.35–0.37 ppm) contents, and consequently high Sr/Y (93.26–94.28), $(La/Yb)_N$ (47.97–51.21), and La/Yb (71.15–75.96) ratios[62] (Fig. 6a, b, c).

The dacites are marked by high SiO_2 (63.01–63.12 wt%), Al_2O_3 (17.65–18.13 wt%), and low K_2O (2.12–2.21 wt%), total alkalis (6.24–6.29 wt%), MgO (0.88–0.94 wt%), and FeO^T (4.15–4.25 wt%) contents. These rocks also belong to the sub-alkaline series and the calc-alkaline series (Fig. 4a, b) and display peraluminous affinities, with high A/CNK ratios of 1.33–1.42 (Fig. 4c). Their $Mg^{\#}$ values range from 29.0 to 31.1, and K_2O/Na_2O ratios vary from 0.52 to 0.54 (Fig. 4d). The dacites show strongly fractionated LREEs relative to HREEs with high $(La/Yb)_N$ (14.41–26.81) values (Fig. 5c). They display negligible Eu anomalies with Eu/Eu* values of 0.91–0.94 (Fig. 5c). The rocks are characterized by enrichment in LILEs and notable depletion in HFSEs (Fig. 5d). Consistent with the rhyolites, the dacites display geochemical affinities to adakitic rocks, as indicated by the high Sr (377.2–595.4 ppm) and low Y (4.52–9.15 ppm) and Yb (0.57–0.71 ppm) contents, and resulting in high Sr/Y (68.08–83.38) $(La/Yb)_N$ (14.41–26.81), and La/Yb (21.38–39.76) ratios[62] (Fig. 6a, b, c).

The granodiorites display high SiO_2 (63.80–65.48 wt%), K_2O (2.65–3.17 wt%), total alkalis (6.45–7.32 wt%), and MgO (1.99–2.45 wt%) but relatively low FeO^T (4.60–5.48 wt%) contents along with elevated K_2O/Na_2O ratios (0.70–0.86) (Fig. 4d). They have moderately high $Mg^{\#}$ values varying from

45.5 to 47.0. On the SiO_2 versus K_2O+Na_2O diagram (Fig. 4a), the samples exhibit sub-alkaline affinity, and on the SiO_2 versus K_2O diagram (Fig. 4b), they fall into the high-K calc-alkaline field. They are peraluminous features with high A/CNK ratios between 1.37 and 1.44 (Fig. 4c). The granodiorites are enriched in LREEs (La_N/Yb_N = 13.48–24.62) (Fig. 5e), exhibit flat HREE patterns (Ho_N/Yb_N = 1.06–1.09), and have negligibly negative Eu anomalies (Eu/Eu*=0.79–0.85). They are enriched in LILE but obviously depleted in HFSEs (Fig. 5f), similar to the aforementioned rhyolites and granodiorites. As shown in Fig. 6a–c, the granodiorites display adakitic signatures including high Sr (390.4–409.0 ppm) and low Y (10.85–13.48 ppm) and Yb (1.11–1.42 ppm) contents, high Sr/Y (29.93–36.62), $(La/Yb)_N$ (13.48–24.62) and La/Yb (19.99–36.52) ratios[62].

The diorites are characterized by high SiO_2 (60.24–61.28 wt%), K_2O (2.33–3.14 wt%), total alkalis (5.02–5.89 wt%), FeO^T (7.27–8.34 wt%), and MgO (3.03–3.13 wt%) contents, along with elevated K_2O/Na_2O ratios (0.84–1.14) (Fig. 4d). The $Mg^{\#}$ values are relatively high, ranging from 41.9 to 45.6. In the classification diagrams, the diorites plot in the sub-alkaline series field (Fig. 4a) and correspond to the high-K calc-alkaline series (Fig. 4b). They also show peraluminous characteristics with high A/CNK ratios of 1.29–1.42 (Fig. 4c). The diorites exhibit LREEs enrichment with $(La/Yb)_N$ and $(La/Sm)_N$ ratios of 4.42–6.05 and 2.63–3.22, respectively (Fig. 5g). They display negative Eu anomalies with Eu/Eu* values of 0.58–0.68 (Fig. 5g). They show enrichment in LILEs and significant depletion in HFSEs (Fig. 5h). The diorites are

classified as non-adakitic rocks[62] (Fig. 6a, b, c), characterized by low Sr (258.0–289.5 ppm) contents, high Y (28.21–29.33 ppm) and Yb (2.94–3.09 ppm) contents, resulting in low Sr/Y (9.04–9.92) and $(La/Yb)_N$ (4.42–6.05) ratios.

Sr–Nd isotope compositions

The Sr–Nd isotope data are listed in Table 3. The initial Sr isotope ratios and $\varepsilon_{Nd}(t)$ values were calculated at 22 Ma for the diorite and 17 Ma for the granodiorite, respectively. The diorites yield relatively high initial $^{87}Sr/^{86}Sr$ ratios of 0.706181–0.706269 and negative age-corrected εNd(t) values of −3.6 to −3.0, with two-stage model ages (T_{2DM}) ranging from 1.08 to 1.23 Ga (Fig. 7a). The granodiorites have relatively high initial $^{87}Sr/^{86}Sr$ ratios of 0.706997 and negative age-corrected εNd(t) values of −3.3 with two-stage model ages (T_{2DM}) of 1.10 Ga (Fig. 7a).

Lu–Hf isotope compositions

Ten zircon grains of the diorites (sample NA12–38–6) display homogeneous Hf isotope compositions (Table 4). The initial $^{176}Hf/^{177}Hf$ ratios are characterized by 0.282660–0.282733, and exhibit negative εHf(t) values ranging from −3.5 to −0.9 with the two-stage model ages of 1.16–1.32 Ga (Fig. 7b).

Discussion

Effects of alteration

The granitoids exhibit variable degrees of hydrothermal alteration, as reflected by their elevated loss on ignition (LOI, to 1100°C) values ranging

from 0.61 to 2.39 wt% (Table 2). To ensure the reliability of the data for petrogenetic and tectonic interpretation, we systematically assessed the mobility of elements during alteration. Most major elements, including SiO_2, Al_2O_3, FeO^T, MgO, CaO, K_2O + Na_2O, and P_2O_5, show no significant correlation with LOI (Supplementary Fig. 1a–h), suggesting that they remained largely immobile during the alteration. In general, REE and HFSE elements and Th are considered relatively immobile, even under intense hydrothermal conditions[63–66]. Consistently, insignificant correlation between LOI and selected elements such as La (REE), Nb, Zr, and Ti (HFSE), and Th (Supplementary Fig. 1i–m) indicates that these elements were not significantly mobilized by post-magmatic or hydrothermal processes. In addition, transition metal elements (Ni, Cr, Co, V) are generally resistant to mobilization during later alteration[67–69]. Therefore, we infer that most major elements and incompatible elements, and particularly their interelement ratios, preserve the original magmatic signatures. These elements and their ratios are thus suitable for discussing petrogenesis, source characteristics, and tectonic implications.

Petrogenesis

Adakitic rhyolite, dacite, and granodiorite

The granodiorite, dacite, and rhyolite in this study exhibit low 10000 × Ga/Al values (2.05–2.35), FeO^T/MgO ratios (2.23–4.85), and (Zr + Nb + Ce + Y) contents (151.91–198.98 ppm), which are consistent with I- and S-type but distinct from A-type granitoids[70] (Fig. 6d, e). S-type granitoids typically

contain Al-rich minerals such as muscovite, garnet, and cordierite, and are characterized by relatively high A/CNK values (up to 1.1)[71–72]. Although the studied samples are peraluminous with elevated A/CNK values of 1.33–1.54, they lack these characteristic Al-rich phases and instead contain clinopyroxene and hornblende (Fig. 3). The I-type granitoids with relatively low Zr saturation temperatures (T_{Zr} = 714–746 °C; Table 2)[73] can be peraluminous, such as peraluminous I-type granitoids from the Lachlan Fold Belt in southeastern Australia[74]. Furthermore, they display a negative correlation between P_2O_5 and SiO_2, which is indicative of I-type rather than S-type granitoids[75] (Fig. 6f). In addition, they have high Sr (377.2–595.4 ppm; most samples > 400 ppm), low Y (4.36–13.48 ppm; < 18 ppm) and Yb (0.35–1.42 ppm; < 1.8 ppm) contents, plotting in the adakitic field on Sr/Y versus Y, $(La/Yb)_N$ versus Yb_N, and La/Yb versus Yb diagrams[62] (Fig. 6a, b, c).

Adakites were originally defined[62, 81] as volcanic rocks derived from partial melting of a young and hot oceanic slab during subduction. They are characterized by high SiO_2 (≥ 56 wt%) and Na_2O (≥ 3.5 wt%; K_2O/Na_2O ≤ 0.4), high Sr (≥ 400 ppm), and low Y (≤ 18 ppm) and Yb (≤ 1.9 ppm) contents with high Sr/Y (> 40) and $(La/Yb)_N$ (> 10) ratios[62, 78–83]. Since that definition, intermediate-felsic rocks that exhibit similar geochemical signatures but form via different petrogenetic mechanisms are termed adakitic rocks. Three main petrogenetic mechanisms have been proposed to account for the origin of adakitic rocks, including: (1) crustal assimilation and fractional crystallization (AFC) processes from parental basaltic magma[76–77];

(2) partial melting of delaminated lower continental crust[79, 84–87]; (3) partial melting of thickened lower continental crust[88–94].

In this study, we infer that the granodiorite, dacite, and rhyolite are not typical adakites, but adakitic rocks that share similar geochemical signatures with typical adakites. Tectonic reconstructions indicate that the Neo-Tethys Ocean had already closed by the Miocene in the Zagros Orogen belt of Iran[2, 4–7], marking the termination of oceanic subduction. Consequently, it is unlikely that these rocks originated from the partial melting of subducted Neo-Tethys oceanic crust. Moreover, they exhibit enriched Nd−Sr isotopic compositions ($\varepsilon Nd(t) = -3.0$, $(^{87}Sr/^{86}Sr)_i = 0.706997$) (Fig. 7a), distinct from those of typical adakites derived from partial melting of subducting oceanic crust, which typically show depleted mantle-like Nd−Sr isotopic signatures[80]. The relatively high and wide Rb/Sr ratios of our samples (0.05−0.29) also differ from those of subducted slab-derived adakites (0.01−0.05)[81]. These rocks contain relatively high Th (9.52−26.85 ppm, with one exception at 2.66 ppm) and K_2O (2.12−3.17 wt%) contents, along with K_2O/Na_2O ratios ranging from 0.52 to 0.86 (Fig. 4d). These compositional features contrast with those of typical slab-derived sodic melts, which are characterized by low Th concentrations (< 3 ppm) and sodic-rich compositions (K_2O/Na_2O ratios < 0.4)[62, 81].

Also, the adakitic rocks in this study cannot be attributed to crustal assimilation and fractional crystallization (AFC) processes from a parental basaltic magma. Because certain highly incompatible elements (e.g., Nb, U,

Ce, and Pb) possess similar partition coefficients, their interelement ratios (e.g., Nb/U and Ce/Pb) tend to remain relatively constant during partial melting or fractional crystallization[95]. Consequently, these ratios are widely used to assess the role of crustal assimilation. The adakitic samples exhibit low Nb/U (1.12–1.78, averaging 1.49) and Ce/Pb ratios (1.70–4.20, averaging 2.61), values even lower than those of typical continental crust (Nb/U = 6 and Ce/Pb = 4)[96], suggesting that crustal assimilation is unlikely to have produced the observed compositional features. Additionally, the absence of a negative correlation between SiO_2 content and Nb/La ratio (Fig. 8a) argues against significant crustal assimilation, as such a trend would be expected if assimilation had occurred[96]. The geochemical trends also provide insights into the role of fractional crystallization. In the Harker diagrams, with increasing MgO content, the adakitic samples show increasing TiO_2, FeO^T, P_2O_5, and Al_2O_3, but decreasing CaO, Na_2O, and K_2O contents, whereas Cr and Ni contents remain constant over a small range of MgO (Supplementary Fig. 2), indicating minor fractional crystallization involving Fe–Ti oxides, apatite, plagioclase, and K-feldspar. Although high-pressure fractionation of garnet from basaltic magma tends to elevate Sr/Y and Dy/Yb ratios in the residual melt, and low-pressure fractionation of hornblende can lower the Dy/Yb ratios[76], the lack of obvious correlations between Sr/Y, Dy/Yb, and SiO_2 contents (Fig. 8b, c) does not support such a scenario. Furthermore, because La is more incompatible than Yb, La/Yb ratios increase with La concentration during partial melting but remain largely constant during fractional

crystallization[97]. On the La/Yb versus La diagram (Fig. 8d), the adakitic samples define a trend consistent with a partial melting process. Thus, we propose that the adakitic rocks were generated by partial melting rather than through the AFC processes from basaltic magma.

The adakitic samples here were most likely derived from partial melting of thickened lower continental crust. They exhibit high SiO_2 (63.01−70.33 wt%), MgO (0.74−2.45 wt%), low Mg# (29−47) values and low Ni (4.56−22.13) contents, which are consistent with typical adakitic rocks derived from partial melting of thickened lower continental crust and experimental results regarding metabasaltic and eclogite melts (1−4 Ga)[97, 99] (Fig. 9a, b, c). Additionally, these samples display elevated Th/Ce (0.10−0.40), Th/La (0.22−0.59), Rb/Sr (0.05−0.29) ratios, which resemble those of adakitic rocks derived from thickened lower crust (Th/Ce = 0.08−0.99, Th/La = 0.15−2.99, Rb/Sr = 0.14−0.20) [100], suggesting a similar source affinity. Moreover, their Nb/Ta (8.06−12.78, average of 10.82) and Zr/Hf (31.36−37.53, average of 35.20) ratios are comparable to those of the lower crust (Nb/Ta = 11, Zr/Hf = 33−36)[101]. Notably, among the adakitic rocks, the rhyolites show high Cr contents (50.55−156.10 ppm) (Fig. 9d), distinguishing them from typical thickened lower crust-derived adakitic magmas and aligning more closely with those derived from delaminated lower crust. However, adakitic melts generated by partial melting of delaminated lower crust typically interact with mantle peridotite during ascent, resulting in significantly higher Mg# values (> 50) and MgO contents (> 2 wt%, even > 3 wt%), and compatible

element concentrations (e.g., Cr ˃ 50 ppm and Ni ˃ 30 ppm) [93, 97, 99]. In contrast, the rhyolites in this study have low Mg# (32.7−39.8), MgO (0.74−0.84 wt %), and Ni (4.56−5.32 ppm) contents (Fig. 9a, b, c), indicating no significant interaction with mantle peridotite. Therefore, we interpret the decoupled Mg#-Cr-Ni signatures in the rhyolites as reflecting source heterogeneity, possibly involving Cr-rich materials such as residual pyroxenite, which contains pyroxene and Cr-spinel that undergo melting, releasing their enriched Cr into the local melt[102]. The adakitic samples are characterized by low HREE contents, high Sr/Y and $(La/Yb)_N$ ratios, and negligible negative Eu anomalies, features indicative of garnet as a major residual phase in the source. The interpretation is reinforced by the positive correlation between $(Dy/Yb)_N$ and $(La/Yb)_N$ (Fig. 8e). Moreover, the low Nb/Ta (8.06–12.78) and Zr/Sm (26.74-53.08) ratios suggest that amphibolite remained in the residue during partial melting[81] (Fig. 8f). Additionally, adakitic rocks (18.67 Ma) in the central UDMA mentioned above[28] display geochemical similarities to those in this study. Therefore, we infer that both the adakitic rocks from this study and those from previous work (18.67 Ma; Fig. 9a–d) were derived from partial melting of thickened lower crust under amphibolite-bearing eclogite facies conditions. The interpretation that the adakitic rocks in the Kashan area were generated by partial melting of thickened lower crust is strongly supported by recent advances in the study of felsic magma genesis. As demonstrated by numerical modeling and experimental petrology, the emplacement of hot mantle-derived magmas into

the lower crust can provide sufficient heat to trigger partial melting of pre-existing thickened crustal materials, producing adakitic melts[103]. Furthermore, the concept of long-lived, crystal-rich magma reservoirs ("mush zones") in the deep crust has been widely applied to explain the generation and extraction of adakitic melts in collisional orogens, where thickened lower crust undergoes anatexis without significant interaction with the mantle[104].

Non-adakitic diorite

In contrast to the adakitic rocks described above, the diorites exhibit low Sr contents (258.0–289.5 ppm) and high concentrations of Y (28.21–29.33 ppm) and Yb (2.94–3.09 ppm), resulting in low Sr/Y ratios ranging from 9.04 to 9.92. These values plot within the field of the normal arc rocks instead of the adakitic field on Sr/Y versus Y, $(La/Yb)_N$ versus Yb_N, and La/Yb versus Yb diagrams[62] (Fig. 6a, b, c). The diorites exhibit a narrow range of compositional variations (e.g., MgO = 3.03–3.13 wt%), suggesting that crustal contamination and/or fractional crystallization played only a negligible role in their genesis. The diorites display pronounced negative Nb, Ta, and Ti anomalies, which may be indicative of crustal contamination. However, the absence of correlation between SiO_2 and Nb/La suggests insignificant crustal contamination for diorites (Fig. 8a). Further evidence for limited crustal contamination includes their low Nb/U (3.23–4.23, averaging 3.73) and Ce/Pb ratios (0.78–3.82, averaging 2.50), both of which are lower than those of typical continental crust (Nb/U = 6 and Ce/Pb = 4)[96, 101]. Their relatively low Zr/Sm (16.07–20.78) ratios are inconsistent with significant

crustal contamination, given the higher Zr/Sm ratios (ca. 32) characteristic of the continental crust[96]. We therefore infer that the dioritic magmas experienced negligible crustal material contamination during ascent, and their negative Nb and Ta anomalies were inherited from their mantle source. The diorites display coherent variation trends on the Harker diagrams and share a similar shape in the chondrite-normalized REE patterns and trace element variations on the primitive mantle-normalized patterns, indicating a comagmatic origin. On the Harker diagrams (Supplementary Fig. 2), MgO shows no significant correlation with TiO_2, FeO^T, P_2O_5, K_2O, Cr, or Ni, a weak positive correlation with Al_2O_3, and a weak correlation with Na_2O and CaO, suggesting limited fractional crystallization of plagioclase and hornblende in the diorites. This inference is supported by moderate negative Eu anomalies (Eu/Eu* = 0.58–0.68), which point to some degree of plagioclase fractionation. Moreover, on the La/Yb versus La diagram (Fig. 8d), the diorites define a positive trend, consistent with a partial melting control. It is thus inferred that the generation of diorites is more likely to be controlled by partial melting with a limited degree of fractional crystallization involving plagioclase and hornblende.

The diorites are characterized by high La/Ta (27.20–33.27) but low Nb/La (0.37–0.45) ratios, indicating a lithospheric mantle source, because magmas derived from such a source typically have elevated La/Ta ratios > 25 and Nb/La < 0.5[105–106]. This inference is corroborated by their enriched Nd−Hf isotopic compositions, with εNd(t) and εHf(t) values ranging from −3.6 to

−3.0, and from −3.5 to −0.9, respectively (Fig. 7a, b). Additionally, the diorites display high-K calc-alkaline affinities (Fig. 4b) and are enriched in LREEs (La_N/Yb_N = 4.42–6.05) with relatively flat HREEs (Gd_N/Yb_N = 1.32–1.71) (Fig. 5g). They also exhibit pronounced enrichment in LILEs alongside marked negative Nb–Ta–Ti anomalies (Fig. 5h). These features are diagnostic of subduction-related magmatism[98, 101]. Consistently, their low Nb/Ta (12.05–13.37) and Zr/Sm (16.07–20.78) ratios also align with a subduction-related origin (Fig. 8f). These geochemical and isotopic signatures collectively suggest that the diorites were generated by the partial melting of the subcontinental lithospheric mantle that had been modified by fluids from subducted sediments. Previous studies have shown that trace element ratios can be employed to examine the contributions of fluid/melt components released from a subducted slab or oceanic sediments[63]. As shown in Fig. 10a, the diorites have low Nb/La ratios (0.37–0.45), reflecting the contribution of fluids released from recycled sediment/slab[107]. They also display low Nb/Zr (0.09–0.11) and Th/Zr (0.08–0.10) ratios (Fig. 10b), indicating significant fluid contributions[107]. Additionally, the diorites exhibit negative $\varepsilon_{Nd}(t)$ values (from −3.6 to −3.0) with high Ba/Th (54.49–67.47) ratios, indicating the involvement of fluids released from sediments[62] (Fig. 10c). In the La/Sc versus Co/Th diagram[108] (Fig. 10d), the diorites exhibit low La/Sc ratios (0.89–1.34), indicating that the recycled sediments are of oceanic subducted origin with La/Sc ratios below 1.5[108]. The low Co/Th ratios (1.64–2.18) of the diorites indicate a felsic to intermediate provenance for the oceanic

sediments. The relatively low Rb/Sr ratios (0.26–0.51) and the wide range of Ba/Rb ratios (3.77–7.77) for the diorites indicate an amphibole-bearing source (Fig. 10e)[81]. The modeling results of mantle melting using Dy/Yb versus La/Yb ratios indicate that the diorites were generated by low-degree (approximately 3–5%) partial melting of enriched amphibole-bearing spinel lherzolite (Fig. 10f). In summary, we propose that the diorites were likely derived from an enriched mantle source, specifically, subcontinental lithospheric mantle, within the stability field of amphibole-bearing spinel through relatively low-degree (3–5%) partial melting.

Implications for geodynamic processes

The early Miocene magmatism was widespread in the UDMA, and extensive research has been conducted on this igneous activity in recent years[13–26]. Nevertheless, the deep geodynamic processes responsible for the formation of these rocks remain controversial. Some researchers have proposed subduction-related processes prior to the initial Arabia-Eurasia collision (ca. 25–23 Ma)[11, 16, 55], interpreting subduction-related geochemical signatures (depletions in Nb, Ta, and Ti) of the Miocene rocks as evidence of subduction processes during the final stage, which lasted into the early Miocene[11, 14, 27, 24, 55]. Others, however, attribute the Oligocene OIB-type magmatism (ca. 37 Ma)[14, 16] combined with the late Miocene shoshonite to post-collisional extension following the Oligocene collision (ca. 37–23 Ma)[32–34, 36–39]. Our new data from the Kashan area helps discriminate between these models as follows.

According to the aforementioned discussion, the non-adakitic diorites exhibit high-K calc-alkaline affinities, enrichment in LREEs and LILEs, significant depletion in HFSEs, and enriched Nd–Hf isotopic compositions. They were most likely derived from an enriched subcontinental lithospheric mantle in the amphibole-bearing spinel facies that has been metasomatized by subduction-related fluids. Generally, the stability field of amphibole-bearing spinel for the diorites indicates partial melting of subcontinental lithospheric mantle at shallow depth (< 70 km)[109] within an extensional setting triggered by upwelling of the underlying hot asthenospheric mantle. Based on the results of this study and previous works, the upwelling and partial melting of the hot asthenospheric mantle were indeed induced by rollback of the subducted Neo-Tethys Ocean slab during the Oligocene in UDMA, as OIB-type magmatism of Oligocene age in the region has been linked to the slab rollback[14, 16, 20] (Fig. 11a). Moreover, studies from major orogenic belts worldwide, including the Alps, the Dabie Mountains, the Junggar terrane, and the Aegean Islands[110], among other examples, demonstrate that slab rollback and breakoff are common processes in subduction–collision systems. Therefore, we suggest that the non-adakitic diorites may represent a response to the final breakup of the subducted Neo-Tethys Ocean slab during the early Miocene (ca. 22 Ma), which resulted in upwelling of hot asthenospheric mantle and consequently partial melting of the subcontinental lithospheric mantle. This event marked the termination of slab subduction and the initial collision between Arabia and Eurasia in Iran

(Fig. 11b).

In contrast, the adakitic rocks (rhyolites, dacites, and granodiorites) have high SiO_2 contents and low $Mg^{\#}$ values, display highly fractionated REE patterns with depletion in HFSEs, and feature high Sr but low Y and Yb contents, high Sr/Y and $(La/Yb)_N$ ratios. Thus, we suggest that the adakitic rocks (rhyolites, dacites, and granodiorites) were generated by partial melting of the thickened lower crust during the main collisional stage (ca. 17 Ma) (Fig. 11c).

In summary, the distinct geochemical signatures and petrogenesis, combined with regional magmatic records, we propose a two-stage evolution, namely, slab breakoff at ca. 24–22 Ma induced asthenospheric upwelling and partial melting of the lithospheric mantle, generating the non-adakitic diorites under an extensional setting that marked the initial collision; subsequently, during the main collisional stage at ca. 19–17 Ma, crustal thickening led to partial melting of the lower crust to produce the adakitic rocks (Fig. 11). Additionally, based on the above study, we propose that prior to ca. 17 Ma, the study area had not yet entered the the post-collisional phase.

Conclusions

(1) The diorites are non-adakitic rocks. They were derived from partial melting of an enriched subcontinental lithospheric mantle metasomatized by subduction-related fluids. They formed during the initial Arabia-Eurasia collision associated with the final breakoff of the subducted Neo-Tethys Ocean slab.

(2) The rhyolites, dacites, and granodiorites are adakitic rocks, characterized by high Sr contents, low Y and Yb contents, and high Sr/Y and $(La/Yb)_N$ ratios. They were generated by partial melting of the thickened lower crust during the main collision between the Arabia and Eurasia plates.

(3) A two-stage evolution was proposed in the study area, namely, slab breakoff at ca. 24–22 Ma and main collisional stage at ca. 19–17 Ma.

Acknowledgements

We thank the journal editor, Professor Hai Zhou, and two anonymous reviewers for constructive and helpful comments and suggestions, which helped to improve the manuscript.

Funding

This research was financially supported by the Geological Survey of China (DD20240100710) and the National Natural Science Foundation of China (NSFC programs 42261144669).

Data availability

All data generated or analyzed during this study are available in the four tables in the text.

Competing interests

The authors declare no competing interests.

References

1. Berberian, F. & Berberian, M. Tectono-plutonic episodes in Iran. In: Gupta, H.K., Delany, F.M. (Eds.), Zagros-Hindu Kush-Himalaya Geodynamic Evolution. *AGU, Washington D.C*, 5–32. (1981).
2. Bagheri, S. & Stampfli, G. M. The Anarak, Jandaq and Posht-e-Badam metamorphic complexes in Central Iran: New geological data, relationships and tectonic

implications. *Tectonophysics* 451, 123–155. (2008).
3. Ji, W. Q., Wu, F. Y., Chung, S. L., Li, J. X. & Liu, C. L. Zircon U–Pb geochronology and Hf isotopic constraints on petrogenesis of the Gangdese batholith, southern Tibet. *Chem. Geol.* 262, 229–245. (2009).
4. Zhang, H. R. & Hou, Z. Q. Tectonic evolution and metallogeny of Zagros, Iran. *Acta Geol. Sin.* 89, 1560–1572 (in Chinese with English abstract). (2015)
5. Deevsalar, R. et al. Mesozoic–Cenozoic mafic magmatism in Sanandaj–Sirjan Zone, Zagros Orogen (Western Iran): Geochemical and isotopic inferences from Middle Jurassic and late Eocene gabbros. *Lithos* 284–285, 588–607. (2017).
6. Zhang, H. R., Chen, J. L., Yang, T. N. & Hou, Z. Q., Aghazadeh, M. Jurassic granitoids in the northwestern Sanandaj–Sirjan Zone: Evolving magmatism in response to the development of a Neo-Tethyan slab window. *Gondwana Res.* 62, 269–286. (2018).
7. Shafaii Moghadam, H., Griffin, W. L., Kirchenbaur, M., Garbe-Schönberg, D., Zakie Khedr, M. & Kimura, J. I. Roll-back, extension and mantle upwelling triggered Eocene potassic magmatism in NW Iran. *J. Petrol.* 59 (7), 1417–1465. (2018).
8. Zhu, D. C., Wang, Q., Chung, S. L., Cawood, P. A. & Zhao, Z. D. Gangdese magmatism in southern Tibet and India-Asia convergence since 120 Ma. In: Treloar, P.J., Searle, M.P. (Eds.), Himalayan Tectonics: A Modern Synthesis. *Geol. Soc. Lond. Spec. Publ.* 483, 583–604. (2019).
9. Berberian, M. & King, G. C. P. Towards a paleogeography and tectonic evolution of Iran. *Can. J. Earth Sci*. 18, 210–265. (1981).
10. Ghasemi, A. & Talbot, C. J. A new tectonic scenario for the SanandajeSirjan Zone (Iran). *J. Afr. Earth Sci.* 26, 683–693. (2006).
11. Agard, P. et al. Zagros orogeny: a subduction-dominated process. *Geol. Mag.* 148, 692–725. (2011).
12. Mouthereau, F., Lacombe, O. & Vergés, J. Building the Zagros collisional orogen: timing, strain distribution and the dynamics of Arabia/Eurasia plate convergence. *Tectonophysics* 532, 27–60. (2012).
13. Omrani, J., Agard, P., Whitechurch, H., Benoit, M., Prouteau, P. & Jolivet, L. Arc magmatism and subduction history beneath the Zagros Mountains, Iran: A new report of adakites and geodynamic consequences. *Lithos* 106, 380–398. (2008).
14. Verdel, C., Wernicke, B. P., Hassanzadeh, J. & Guest, B. A Paleogene extensional arc flare-up in Iran. *Tectonics 30*, TC3008. (2011).
15. Kananian, A., Sarjoughian, F., Nadimi, A., Ahmadian, J. & Ling, W. L. Geochemical characteristics of the Kuh-e Dom intrusion, Urumieh–Dokhtar Magmatic Arc (Iran): Implications for source regions and magmatic evolution. *J. Asian Earth Sci.* 90, 137–148. (2014).
16. Shahsavari Alavijeh, B., Rashidnejad-Omran, N. & Corfu, F. Zircon U-Pb ages and emplacement history of the Nodoushan plutonic complex in the central Urumieh-Dokhtar magmatic belt, Central Iran: Product of Neotethyan subduction during the Paleogene. *J. Asian Earth Sci.* 143, 283–295. (2017).
17. Nouri, F. et al. Zircon U-Pb dating, geochemistry and evolution of the Late Eocene Saveh magmatic complex, central Iran: Partial melts of sub-continental lithospheric mantle and magmatic differentiation. *Lithos* 314–315, 274–292. (2018).
18. Sepidbar, F. et al. Across-arc geochemical variations in the Paleogene magmatic belt of Iran. *Lithos* 344–345, 280–296. (2019).
19. Chaharlang, R., Ducea, M. N. & Ghalamghash, J. Geochemical evidences for quantifying crustal thickness over time in the Urumieh-Dokhtar magmatic arc (Iran). *Lithos* 374–375, 105723. (2020).
20. Moghadam, H. S. et al. Roll-back, extension and mantle upwelling triggered Eocene potassic magmatism in NW Iran. *J. Petrol.* 59, 1417–1465. (2018).
21. Moghadam, H. S. et al. Geochronology, geochemistry and petrology of the Oligocene magmatism in SE segment of the UDMB, Iran. *Lithos* 416–417, 106644. (2022).

22. Mokhtari, M. A. A., Kouhestani, H., Pang, K. N., Hsu, S. C., Chung, S. L. & Lee, H. Y. Early Eocene high-Sr/Y magmas from the Urumieh-Dokhtar paleo-arc, Iran: Implications for the origin of high-flux events in magmatic arcs. *Lithos* 416–417, 106656. (2022).
23. Babazadeh, S., Antonio, M. D., Cottle, J. M., Ghalamghash, J., Raeisi, D. & An, Y. J. Constraints from geochemistry, zircon U-Pb geochronology and Hf-Nd isotopic compositions on the origin of Cenozoic volcanic rocks from central Urumieh-Dokhtar magmatic arc, Iran. *Gondwana Res.* 90, 27–46. (2021).
24. Babazadeh, S., Furman, T., Santosh, M., Raeisi, D., Choi, S. H. & Antonio, M. D. Middle to Late Miocene K-rich magmatism in Central Iran: Geochemical characterization of the post-collision mantle beneath the Urumieh–Dokhtar magmatic arc. *Chem. Geol.* 665, 122308. (2024).
25. Alizadeh Noudeh, S., Rolland, Y., Rossi, M., Bruguier, O. & Rahgoshay, M. Eocene high-K magmatic flare-up in a context of south dipping subduction and strike-slip tectonics: Insights from the Talysh Massif, NW Iran. *J. Afr. Earth Sci.* 264, 106045. (2024).
26. Shiva, A. N. et al. Geochronological, isotopic and petrogenetic investigations of Cenozoic Volcanic rocks in the Talysh Massif, NW Iran: Insights for the Eocene magmatic flare-up. *Lithos* 496–497, 107954. (2025).
27. Chiu, H. Y., Chung, S. L., Zarrinkoub, M. H., Mohammadi, S. S., Khatib, M. M. & Iizuka, Y. Zircon U–Pb age constraints from Iran on the magmatic evolution related to Neotethyan subduction and Zagros orogeny. *Lithos* 162–163, 70–87. (2013).
28. Yeganehfar, H., Ghorbani, M. R., Shinjo, R. & Ghaderi, M. Magmatic and geodynamic evolution of Urumieh–Dokhtar basic volcanism, Central Iran: major, trace element, isotopic, and geochronologic implications. *Int. Geol. Rev.* 55(6), 767–786. (2013).
29. Ghorbani, M. R., Graham, I. T. & Ghaderi, M. Oligocene–Miocene geodynamic evolution of the central part of Urumieh-Dokhtar Arc of Iran. *Int. Geol. Rev.* 56(8), 1039–1050. (2014).
30. Dokuz, A. A slab detachment and delamination model for the generation of Carboniferous high-potassium I-type magmatism in the Eastern Pontides, NE Turkey: The Kose composite pluton. *Gondwana Res.* 19, 926–944. (2011).
31. Babazadeh, S. et al. Late Oligocene–Miocene mantle upwelling and interaction inferred from mantle signatures in gabbroic to granitic rocks from the Urumieh–Dokhtar arc, south Ardestan, Iran. *Int. Geol. Rev.* 59(12), 1590–1608. (2017).
32. Shafiei, B., Haschke, M. & Shahabpour, J. Recycling of orogenic arc crust triggers porphyry Cu mineralization in Kerman Cenozoic arc rocks, southeastern Iran. *Miner. Deposita.* 44, 265–283. (2009).
33. Dargahi, S., Arvin, M., Pan, Y. M. & Babaei, A. Petrogenesis of post-collisional A-type granitoids from the Urumieh–Dokhtar magmatic assemblage, Southwestern Kerman, Iran: Constraints on the Arabian–Eurasian continental collision. *Lithos* 115, 190–204. (2010).
34. Rezaeian, M., Carter, A., Hovius, N. & Allen, M. B. Cenozoic exhumation history of the Alborz Mountains, Iran: New constraints from low-temperature chronometry. *Tectonics* 31. (2012).
35. Pirouz, M., Avouac, J. P., Hassanzadeh, J., Kirschvink, J. L. & Bahroudi, A. Early Neogene foreland of the Zagros, implications for the initial closure of the Neo-Tethys and kinematics of crustal shortening. *Earth Planet. Sci. Lett.* 477, 168–182. (2017).
36. Haghighi Bardineh, S. N., Sahamieh, R. Z., Zamanian, H. & Khalaji, A. A. Geochemical, Sr-Nd isotopic investigations and U-Pb zircon chronology of the Takht granodiorite, west Iran: Evidence for postcollisional magmatism in the northern part of the Urumieh-Dokhtar magmatic assemblage. *J. Afr. Earth Sci.* 139, 354–366. (2018).
37. Stern, R. J., Moghadam, H. S., Pirouz, M. & Mooney, W. The geodynamic evolution of Iran. *Annu. Rev. Earth Planet. Sci.* 49, 9–36. (2021).

38. Fedele, L., Ghazi, J. M., Agostini, S., Ronca, S., Innocenzi, F. & Lustrino, M. Concurrent adakitic and non-adakitic Late Miocene-Quaternary magmatism at the Sahand volcano, Urumieh-Dokhtar Magmatic Arc (NW Iran). *Lithos* 458–459, 107344. (2023).
39. Fedele, L., Rahimzadeh, B., Salari, G., Agostini, S., Masoudi, F. & Lustrino, M. A Showcase of Igneous Processes in the Urumieh-Dokhtar Magmatic Arc: the Miocene-Quaternary Collisional Magmatism of the Bijar-Qorveh Area, Northwest Iran. *J. Petrol.* 63, 1–28. (2022).
40. Moradi, S., Christiansen, E. H., Jiang, S. Y. & Ghorbani, M. R. Petrogenesis and tectonic implications of Cenozoic mafic volcanic rocks in the Kahak area of central Urumieh–Dokhtar magmatic arc, Iran. *J. Asian Earth Sci.* 239, 105404. (2022).
41. Moghaddam, M. J. & Karimpour, M. H. Eocene non-mineralization to Miocene porphyry copper mineralization-related magmatism in the Urumieh–Dokhtar magmatic arc, Iran. *J. Geochem. Explor.* 255, 107338. (2023).
42. Rossetti, F. et al. Adakite differentiation and emplacement in a subduction channel: the late Paleocene Sabzevar magmatism (NE Iran). *Geol. Soc. Am. Bull.* 126, 317–343. (2014).
43. Rabiee, A. et al. Long-lived, Eocene-Miocene stationary magmatism in NW Iran along a transform plate boundary. *Gondwana Res.* 85, 237–262. (2020).
44. McInnes, B. I. A., Evans, N. J., Belousova, E. & Griffin, W. L. Porphyry copper deposits of the Kerman belt, Iran: timing of mineralization and exhumation processes. *CSIRO Scientific Research Report*. 41. (2003).
45. McInnes, B. I. A., Evans, N. J., Fu, F. Q. & Garwin, S. Application of thermochronology to hydrothermal ore deposits. *Rev. Mineral. Geochem.* 58, 467–498. (2005).
46. Aghazadeh, M., Castro, A., Badrzadeh, Z. & Vogt, K. Post-collisional polycyclic plutonism from the Zagros hinterland: the Shaivar Dagh plutonic complex, Alborz belt, Iran. *Geol. Mag.* 148, 980–1008. (2011).
47. Aghazadeh, M., Hou, Z. Q, Badrzadeh, Z. & Zhou, L. Temporal–Spatial distribution and tectonic setting of porphyry copper deposits in Iran: Constraints from zircon U–Pb and molybdenite Re–Os geochronology. *Ore Geol. Rev.* 70, 385–406. (2015).
48. Honarmand, M. et al. Laser-ICP-MS U–Pb zircon ages and geochemical and Sr–Nd–Pb isotopic compositions of the Niyasar plutonic complex, Iran: constraints on petrogenesis and tectonic evolution. *Int. Geol. Rev.* 56, 104–132. (2014).
49. Ayati, F., Yavuz, F., Asadi, H. H., Richards, J. P. & Jourdan, F. Petrology and geochemistry of calc-alkaline volcanic and subvolcanic rocks, Dalli porphyry copper–Gold deposit, Markazi Province, Iran. *Int. Geol. Rev.* 55, 158–184. (2013).
50. Raeisi, D., Mirnejad, H., McFarlane, C., Sheibi, M. & Babazadeh, S. Geochemistry and zircon U-Pb geochronology of Miocene plutons in the Urumieh-Dokhtar magmatic arc, east Tafresh, Central Iran. *Int. Geol. Rev.* 62, 1815–1827. (2020).
51. Aliyari, F., Afzal, P., Harati, H. & Hou, Z. Q. Geology, mineralogy, ore fluid characteristics, and $^{40}Ar/^{39}Ar$ geochronology of the Kahang Cu-(Mo) porphyry deposit, Urumieh-Dokhtar Magmatic Arc, Central Iran. *Ore Geol. Rev.* 116, 103238. (2020).
52. Khaksar, T., Rashidnejad-Omran, N., Chen, F. K., Song, S. G. & Ghaderi, M. Zircon U-Pb Ages and Magmatic History of the Kashan Plutons in the Central Urumieh-Dokhtar Magmatic Arc, Iran: Evidence for Neotethyan Subduction during Paleogene-Neogene. *J. Earth Sci.* 31, 53–68. (2020).
53. Neill, I., Meliksetian, K., Allen, M. B., Navasardyan, G. & Kuiper, K. Petrogenesis of mafic collision zone magmatism: the Armenian sector of the Turkish-Iranian Plateau. *Chem. Geol.* 403, 24–41. (2015).
54. Fazlnia, A. Origin and magmatic evolution of the Quaternary syn-collision alkali basalts and related rocks from Salmas, northwestern Iran. *Lithos* 344–345, 297–310.

(2019).
55. Agard, P., Omrani, J., Jolivet, L. & Mouthereau, F. Convergence history across Zagros (Iran): constraints from collisional and earlier deformation. *Int. J. Earth Sci.* 94, 401–419. (2005).
56. Yuan, H. L. et al. Simultaneous determinations of U–Pb age, Hf isotopes and trace element compositions of zircon by excimer laser-ablation quadrupole and multiple-collector ICPMS. *Chem. Geol.* 247, 100–118. (2008).
57. Ludwig, K. R. User's manual for Isoplot 3.0: a geochronological toolkit for Microsoft Excel. *Berkeley Geochronol. Cent. Spec. Publ.* 4, 71. (2003).
58. Elhlou, S., Belousova, E., Griffin, W.L., Pearson, N.J., O'Reilly, S.Y. Trace element and isotopic composition of GJ-red zircon standard by laser ablation. *Geochim. Cosmochim. Acta.* 70 (18), A158. (2006).
59. Hou, K. J., Li, Y. H., Zou, T. R., Qu, X. M., Shi, Y. R. & Xie, G. Q. Laser ablation-MC-ICPMS technique for Hf isotope microanalysis of zircon and its geological applications. *Acta Petrol. Sin.* 23, 2595–2604 (in Chinese with English abstract). (2007).
60. Chen, J. L., Xu, J. F., Wang, B. D., Kang, Z. Q. & Li, J. Origin of Cenozoic alkaline potassic volcanic rocks at KonglongXiang, Lhasa terrane, Tibetan Plateau: products of partial melting of a mafic lower-crustal source? *Chem. Geol.* 273, 286–299. (2010).
61. Hoskin, P. W. O. & Schaltegger, U. The composition of zircon and igneous and metamorphic petrogenesis. *Rev. Mineral. Geochem.* 53, 27–62. (2003).
62. Defant, M. J. & Drummond, M. S. Derivation of some modern arc magmas by melting of young subducted lithosphere. *Nature* 347 (6294), 662–665. (1990).
63. Hawkesworth, C. J., Turner, S. P., McDermott, F., Peate, D. W. & van Calsteren, P. U–Th isotopes in arc magmas: implications for element transfer from subducted crust. *Science* 276, 551–555. (1997).
64. Kerrich, R., Polat, A., Wyman, D. & Hollings, P. Trace element systematics of Mg-, to Fe-tholeiitic basalt suites of the Superior Province: implications for Archean mantle reservoirs and greenstone belt genesis. *Lithos* 46, 163–187. (1999).
65. Polat, A. et al. Trace element systematics of the Neoarchean Fiskenæsset anorthosite complex and associated meta-volcanic rocks, SW Greenland: Evidence for a magmatic arc origin. *Precambrian Res.* 175, 87–115. (2009).
66. Zhong, J. et al. Major and trace element migration and metallogenic processes of the Xinshuijing U-Th deposit in the Longshoushan metallogenic belt, Gansu Province. *Geol. China.* 43, 1393–1408 (in Chinese with English abstract). (2016).
67. Floyd, P. A. & Winchester, J. A. Identification and discrimination of altered and metamorphosed volcanic rocks using immobile elements. *Chem. Geol.* 21, 291–306. (1978).
68. Jochum, K. P., Arndt, N. T. & Hofmann, A. W. Nb-Th-La in komatiites and basalts: constraints on komatiite petrogenesis and mantle evolution. *Earth Planet. Sci. Lett.* 107, 272–289. (1991).
69. Kiipli, T., Hints, R., Kallaste, T., Verš, E. & Voolma, M. Immobile and mobile elements during the transition of volcanic ash to bentonite–an example from the early Palaeozoic sedimentary section of the Baltic Basin. *Sediment. Geol.* 347, 148–159. (2017).
70. Whalen, J. B., Currie, K. L. & Chappell, B. W. A-type granites: geochemical characteristics, discrimination and petrogenesis. *Contrib. Mineral. Petrol.* 95, 407–419. (1987).
71. Chappell, B. W. & White, A. J. R. Two contrasting granite types. *Pacific Geo.* 7, 173–174. (1974).
72. Sylvester, P. J. Post-Collisional strongly peraluminous granites. *Lithos* 45, 29–44. (1998).
73. Watson, E. B. & Harrison, T. M. Zircon saturation revisited: temperature and composition effects in a variety of crustal magma types. *Earth Planet. Sci. Lett.* 64, 295–304. (1983).

74. Chappell, B. W., Bryant, C. J. & Wyborn, D. Peraluminous I-type granites. *Lithos* 153, 142–153. (2012).
75. Clemens, J. D. S-type granitic magmas: petrogenetic issues, models and evidence. *Earth Sci. Rev.* 61 (1–2), 1–18. (2003).
76. Castillo, P. R., Janney, P. E. & Solidum, R. U. Petrology and geochemistry of Camiguin island, southern Philippines: insights to the source of adakites and other lavas in a complex arc setting. *Contrib. Mineral. Petrol.* 134, 33–51. (1999).
77. Macpherson, C. G., Dreher, S. T. & Thirlwall, M. F. Adakites without slab melting: high pressure differentiation of island arc magma, Mindanao, the Philippines. *Earth Planet. Sci. Lett.* 243, 581–593. (2006).
78. Sajona, F. G. et al. Initiation of subduction and the generation of slab melts in western and eastern Mindanao, Philippines. *Geology* 21, 1007–1010. (1993).
79. Wang, Q. et al. Eocene melting of subducting continental crust and early uplifting of central Tibet: evidence from central-western Qiangtang high-K calc-alkaline andesites, dacites and rhyolites. *Earth Planet. Sci. Lett.* 272, 158–171. (2008).
80. Gutscher, M. A., Maury, R., Eissen, J. P. & Bourdon, E. Can slab melting be caused by flat subduction? *Geology* 28, 535–538. (2000).
81. Martin, H., Smithies, R. H., Rapp, R., Moyen, J. F. & Champion, D. An overview of adakite, tonalite–trondhjemite–granodiorite (TTG), and sanukitoid: relationships and some implications for crustal evolution. *Lithos* 79, 1–24. (2005).
82. Moyen, J. F. High Sr/Y and La/Yb ratios: the meaning of the “adakitic signature”. *Lithos* 112, 556–574. (2009).
83. Reich, M., Parada, M. A., Palacios, C., Dietrich, A., Schultz, F. & Lehmann, B. Adakite like signature of late Miocene intrusions at the Ls Pelanbres giant porphyry copper deposit in the Andes of central Chile: metallogenic implications. *Miner. Deposita.* 38, 876–885. (2003).
84. Gao, S. et al. Recycling lower continental crust in the North China craton. *Nature* 432, 892–897. (2004).
85. Kay, R. W. & Kay, S. M. Delamination and delamination magmatism. *Tectonophysics* 219, 177–189. (1993).
86. Wang, Q. et al. Petrogenesis of adakitic porphyries in an extensional tectonic setting, Dexing, South China: implications for the genesis of porphyry copper mineralization. *J. Petrol.* 47, 119–144. (2006).
87. Xu, J. F., Shinjio, R., Defant, M. J., Wang, Q. & Rapp, R. P. Origin of Mesozoic adakitic intrusive rocks in the Ningzhen area of east China: partial melting of delaminated lower continental crust? *Geology* 30, 1111–1114. (2002).
88. Atherton, M. P. & Petford, N. Generation of sodium-rich magmas from newly underplated basaltic crust. *Nature* 362, 144–146. (1993).
89. Chung, S. L. et al. Adakites from continental collision zones: melting of thickened lower crust beneath southern Tibet. *Geology* 31, 1021–1024. (2003).
90. Condie, K. C. TTGs and adakites: are they both slab melts? *Lithos* 80, 33–44. (2005).
91. Streck, M. J., Leeman, W. P. & Chesley, J. High-Mg andesite from Mount Shasta: a product of magma mixing and contamination, not a primitive mantle melt. *Geology* 35, 351–354. (2007).
92. Wang, Q., McDermott, F., Xu, J. F., Bellon, H. & Zhu, Y. T. Cenozoic K-rich adakitic volcanic rocks in the Hohxil area, northern Tibet: lower-crustal melting in an intracontinental setting. *Geology* 33, 465–468. (2005).
93. Wang, Q. et al. Early Cretaceous adakitic granites in the Northern Dabie Complex, central China: implications for partial melting and delamination of thickened lower crust. *Geochim. Cosmochim. Acta.* 71 (10), 2609–2636. (2007).
94. Xiong, X. L. et al. Extremely high-Na adakite-like magmas derived from alkali-rich basaltic underplate: the Late Cretaceous Zhantang andesites in the Huichang Basin, SE China. *Geochem. J.* 37, 233–252. (2003).

95. Baker, J. A., Menzies, M. A. & Thirlwall, M. F. Petrogenesis of Quaternary intraplate volcanism, Sana'a Yenmen: Implication and polybaric melt hybridization. *J. Petrol.* 38, 1359−239. (1997).
96. Taylor, S. R. & McLennan, S. M. The Continental Crust: Its Composition and Evolution. *Oxford Press, Blackwell*. 1–312. (1985).
97. Long, X. P. et al. Partial melting of thickened continental crust in central Tibet: Evidence from geochemistry and geochronology of Eocene adakitic rhyolites in the northern Qiangtang Terrane. *Earth Planet. Sci. Lett.* 414, 30–44. (2015).
98. Tamura, Y. et al. Mission immiscible: distinct subduction components generate two primary magmas at Pagan Volcano, Mariana Arc. *J. Petrol.* 55, 63–101. (2014).
99. Zhang, J. B. et al. Neoproterozoic slab window in the western Yangtze Block, South China: Evidence from adakitic granodiorites, gabbro-diorites and high-K granites in the Panxi arc belt. *J. Asian Earth Sci.* 259, 105859. (2024).
100. Hou, Z. Q., Gao, Y. F., Qu, X. M., Rui, Z. Y. & Mo, X. X. Origin of adakitic intrusives generated during mid-Miocene east-west extension in southern Tibet. *Earth Planet. Sci. Lett.* 220, 139–155. (2004).
101. Sun, S. S. & McDonough, W. F. Chemical and isotopic systematics of ocean basalt: implications for mantle composition and processes. *Geol. Soc. Lond. Spec. Publ.* 42, 313–345. (1989).
102. Moazzen, M., Ahangari, M., Oberhnsli, R. & Altenberger, U. Mineral chemistry and alteration patterns of Cr-spinel in serpentinized peridotites from NW Iran. *J. Asian Earth Sci.* 11, 100178. (2024).
103. Annen, C., Blundy, J. D. & Sparks, R. S. J. The genesis of intermediate and silicic magmas in deep crustal hot zones. *J. Petrol*. 47, 505–539. (2006).
104. Bachmann, O. & Huber, C. Magma reservoirs: What are they, how do they evolve, and why are they so mushy? *Am. Mineral.* 101, 2381–2402. (2016).
105. Condie, K. C. & Shearer, C. K. Tracking the evolution of mantle sources with incompatible element ratios in stagnant-lid and plate-tectonic planets. *Geochim. Cosmochim. Acta.* 213, 47–62. (2017).
106. Condie, K. C. Incompatible element ratios in oceanic basalts and komatiites: tracking deep mantle sources and continental growth rates with time. *Geochem. Geophys. Geosyst*. 4, 1005. (2003).
107. Hofmann, A. W. Mantle geochemistry: the message from oceanic volcanism. *Nature* 385, 219–229. (1997).
108. Armstrong-Altrin, J. S. et al. Geochemistry of the Jurassic and upper Cretaceous shales from the Molango Region, Hidalgo, eastern Mexico: Implications of source area weathering, provenance, and tectonic setting. *C. R. Geosci.* 345(4), 185–202. (2013).
109. Furman, T. & Graham, D. Erosion of lithospheric mantle beneath the East African Rift system: geochemical evidence from the Kivu volcanic province. *Lithos* 48, 237–262. (1999).
110. von Blanckenburg, F. & Davis, J. H. Slab breakoff: a model for syncollisional magmatism and tectonics in the Alps. *Tectonics* 14, 120–131. (1995).

Figure captions

Fig. 1 (a) Geological sketch map showing the distribution of magmatic rocks in Iran[14, 27]; (b) Sketch geological map of Miocene granitoids from the Kashan area (modified from 1: 100,000 geological map of the Kashan area, Geological Survey of Iran).

Fig. 2 Microphotographs showing the major minerals and textures of the studied granitoids from the Kashan area. (a, b) Plagioclase, sanidine, Quartz, and biotite in the rhyolites; (c, d) Plagioclase and K-feldspar with minor clinopyroxene in the dacites; (e, f) plagioclase, K-feldspar, biotite, hornblende, and Quartz in the granodiorites; (g, h) plagioclase and hornblende in the diorites. Pl = Plagioclase, Sa = sanidine, Kf = K-feldspar, Qz = Quartz, Bi = biotite, Hb = hornblende, Cpx = clinopyroxene.

Fig. 3 CL image (a) and U–Pb concordia (b, c) and mean ages diagrams (d) for zircon grains from the diorites. The spots of U–Pb data are shown with the yellow circles, and the spots of Lu–Hf data are shown with the pink circles.

Fig. 4 Diagrams of (a) SiO_2 versus $K_2O + Na_2O$; (b) SiO_2 versus K_2O; (c) A/CNK versus A/NK; (d) K_2O versus Na_2O.

Fig. 5 (a, c, e, g) Chondrite-normalized REE patterns and (b, d, f, h) primitive mantle normalized incompatible element patterns for the rhyolites, dacites, granodiorites, and diorites. The normalization values are from Sun et al.[101].

Fig. 6 Diagrams of discrimination for the rhyolites, dacites, granodiorites, and diorites. (a) the Sr/Y versus Y[62]; (b) $(La/Yb)_N$ versus Yb_N[62]; (c) La/Yb versus Yb[62]; (d) FeO^T/MgO versus 10000 × Ga/Al[70]; (e) $(K_2O + Na_2O)/CaO$ versus (Zr + Nb + Ce + Y)[70]; (f) P_2O_5 versus SiO_2 diagram[71].

Fig. 7 (a) Sr–Nd isotopic diagram of the granodiorites and diorites; (b) zircon εHf(t) value versus U–Pb age of the diorites.

Fig. 8 Diagrams of (a) SiO_2 versus Nb/La; (b) SiO_2 versus Sr/Y; (c) SiO_2 versus Dy/Yb; (d) La versus La/Yb; (e) $(La/Yb)_N$ versus $(Dy/Yb)_N$; (f) Zr/Sm versus

Nb/Ta[81].

Fig. 9 Diagrams of (a) SiO_2 versus $Mg^{\#}$; (b) SiO_2 versus MgO; (c) SiO_2 versus Ni; (d) SiO_2 versus Cr. The diagrams are after[62, 81, 93].

Fig. 10 Diagrams of (a) Nb/La versus Th/Nb; (b) Th/Zr versus Nb/Zr; (c) εNd(t) versus Ba/Th; (d) La/Sc versus Co/Th; (e) Rb/Sr versus Ba/Rb; (f) Dy/Yb versus La/Yb for the diorites illustrating geochemical modeling results. Gt lh: garnet lherzolite, Amp Gt lh: amphibole-bearing garnet lherzolite, Sp lh: spinel lherzolite; Amp Sp lh: amphibole-bearing spinel lherzolite. D values are from http://earthref.org/database. Source mineralogy is 50% olivine, 30% orthopyroxene, 15% clinopyroxene, 5% garnet for garnet lherzolite; Source mineralogy is 50% olivine, 21% orthopyroxene, 20% clinopyroxene, 5% garnet, 4% amphibole for amphibole-bearing garnet lherzolite; Source mineralogy is 50% olivine, 35% orthopyroxene, 10% clinopyroxene, 5% spinel for spinel lherzolite; Source mineralogy is 50% olivine, 22% orthopyroxene, 20% clinopyroxene, 5% spinel, 3% amphibole for amphibole-bearing spinel lherzolite. The primitive mantle and enriched mantle compositions are from[101].

Fig. 11 Schematic cartoons showing the proposed model of the geodynamic processes of central UDMA.

Table captions

Table 1. Zircon U–Pb analytical data of diorite (NA12–38–6) in the Kashan area.

Table 2. Bulk rock composition of major (wt%) and trace elements (ppm) of

samples in the Kashan area.

Table 3. Sr–Nd isotopic compositions of samples in the Kashan area.

Table 4. Lu–Hf isotopic compositions of diorite (NA12–38–6) in the Kashan area.

Supplementary materials

Supplementary Table 1 Sample information in the Kashan area.

Supplementary Fig. 1 LOI (loss on ignition) versus major and trace elements composition for the rhyolites, dacites, granodiorites, and diorites.

Supplementary Fig. 2 Plots of MgO versus several major and trace elements for the rhyolites, dacites, granodiorites, and diorites.

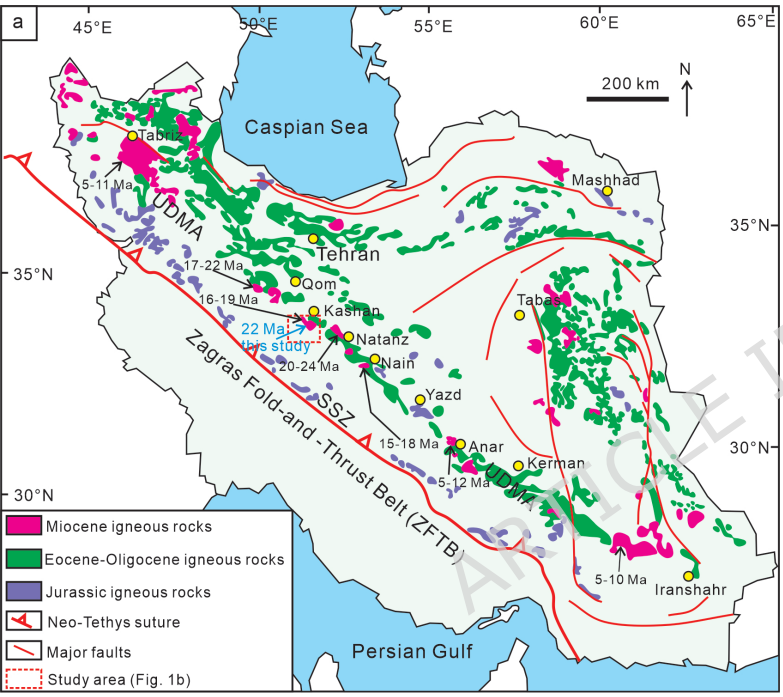

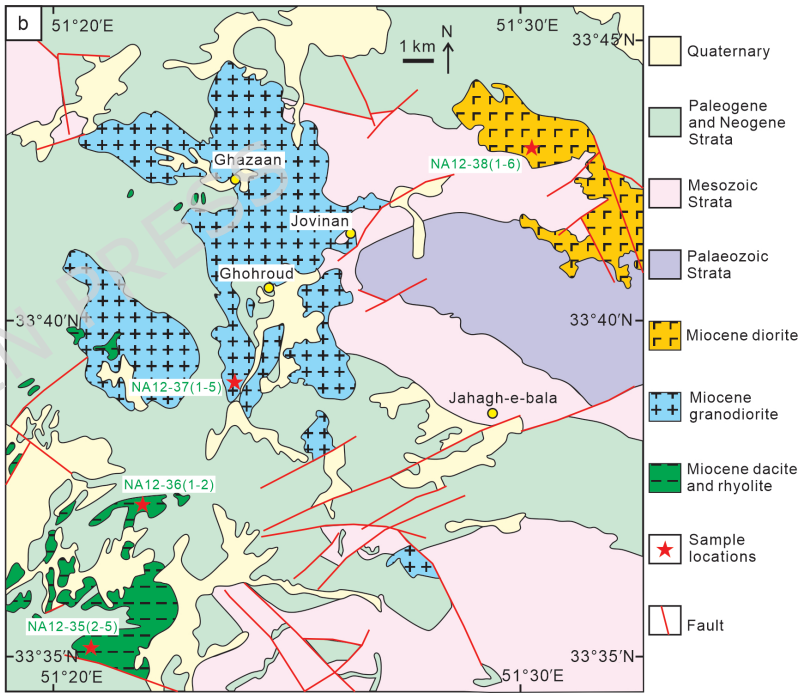

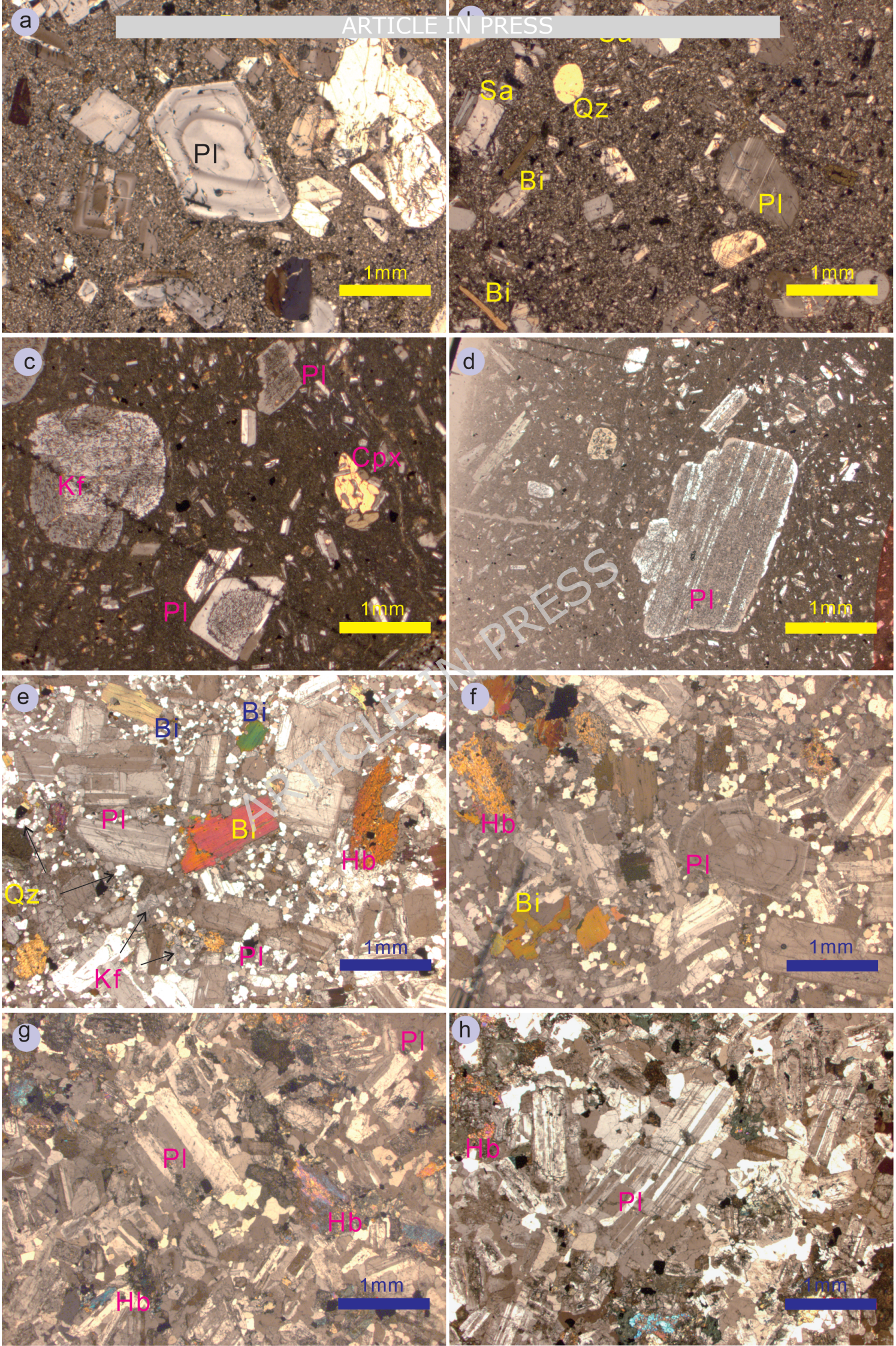

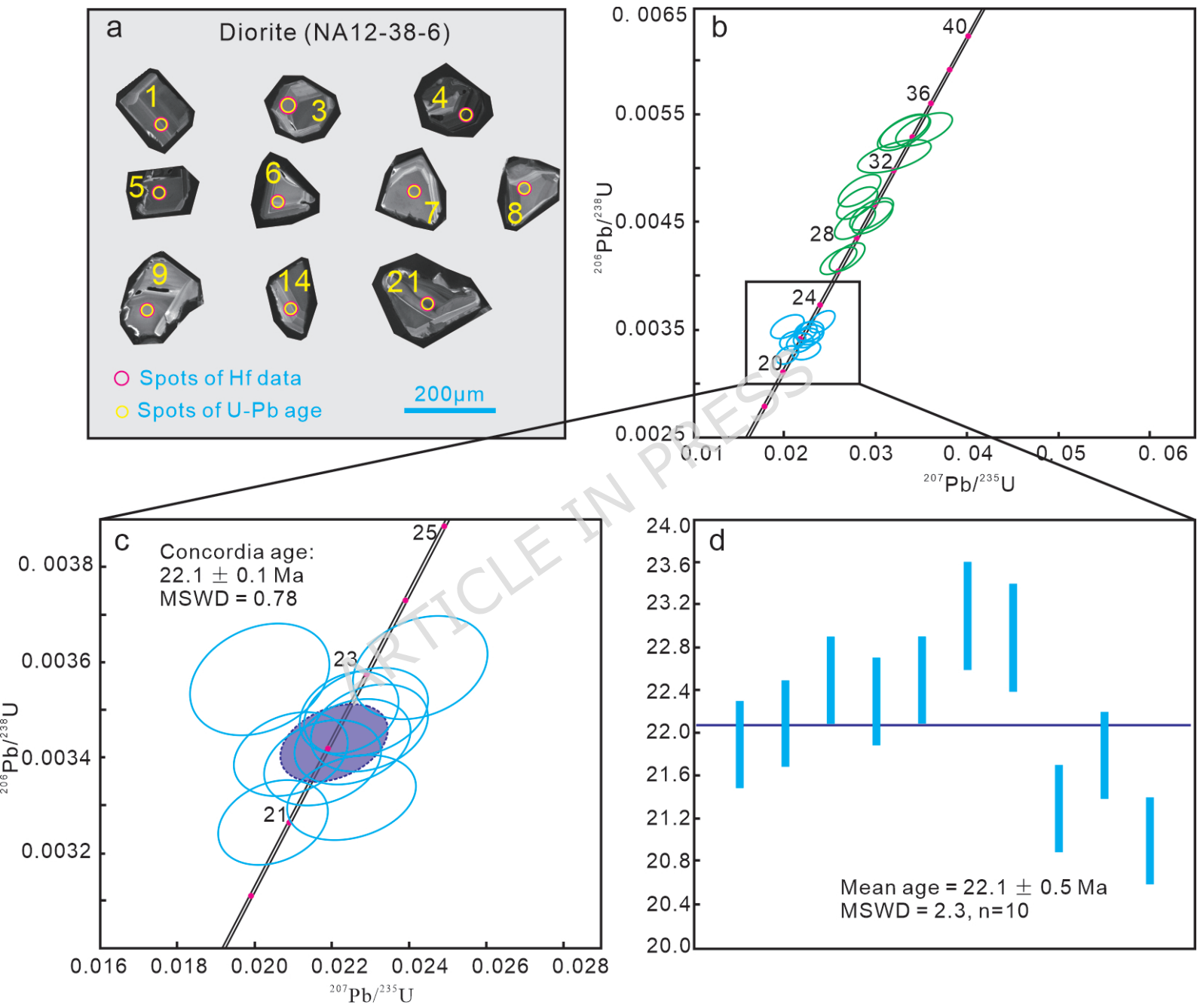

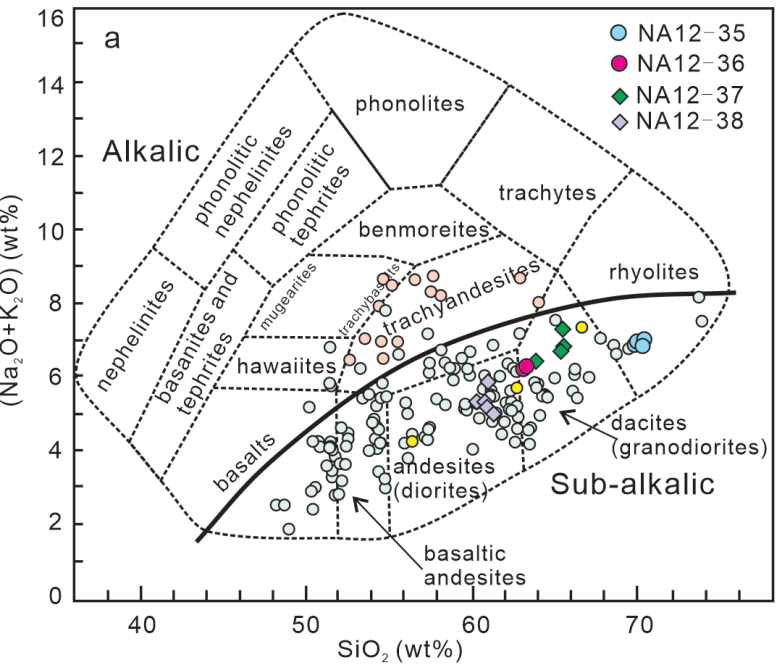

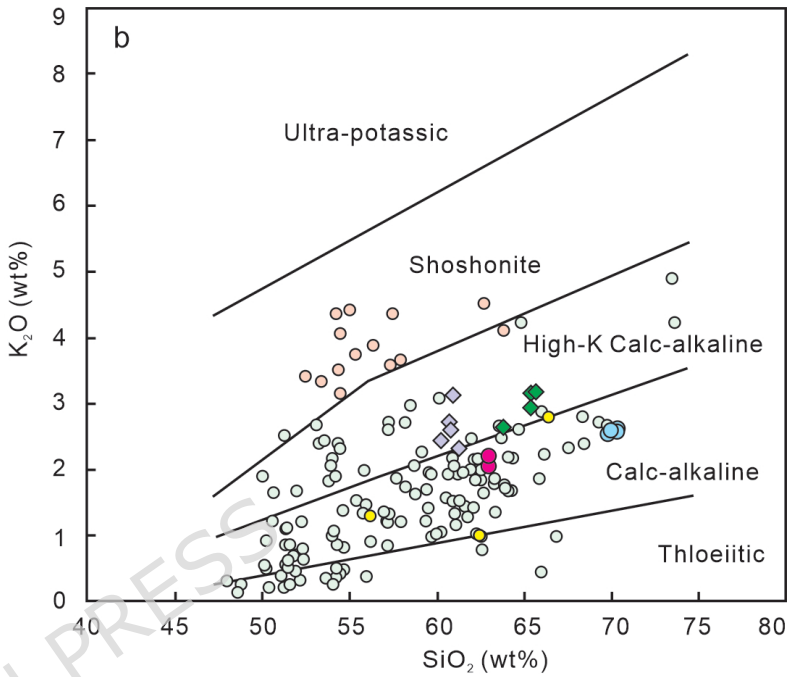

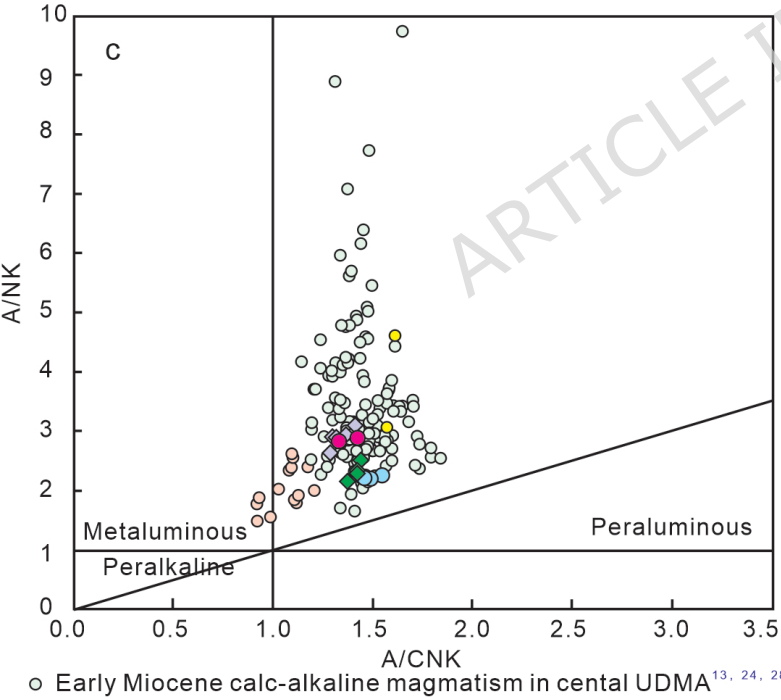

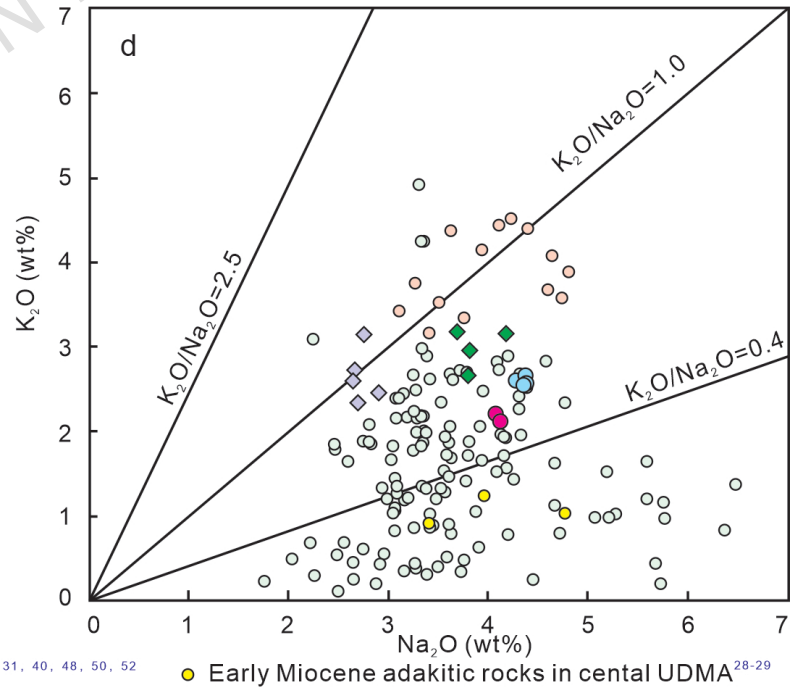

Early Miocene calc-alkaline magmatism in cental UDMA[13, 24, 28, 31, 40, 48, 50, 52]

Early Miocene adakitic rocks in cental UDMA[28-29]

Late Miocene K-rich magmatism from Ardestan and Kahang areas in the cental UDMA[24]

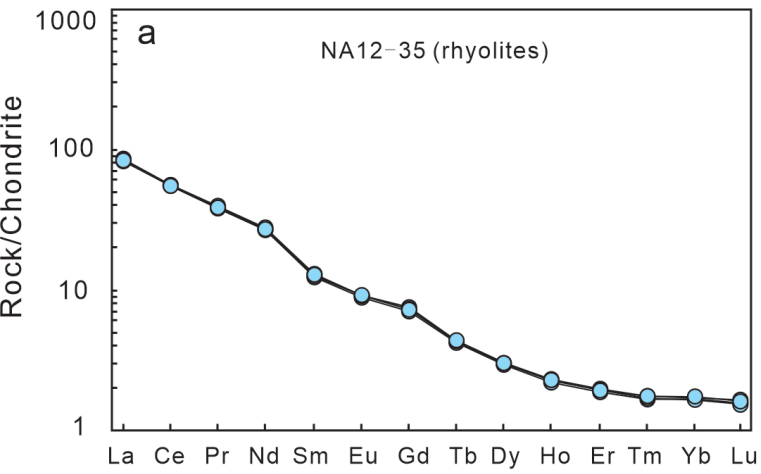

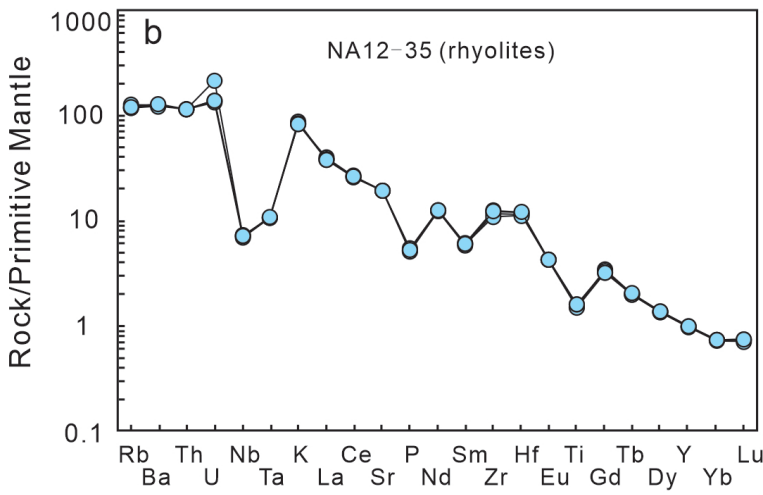

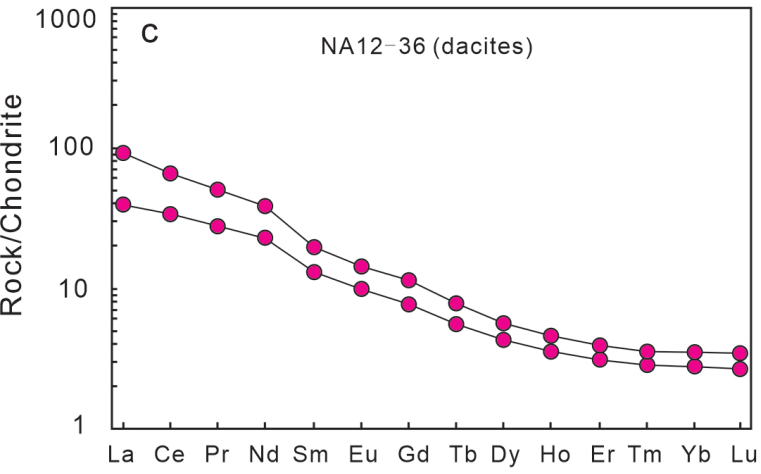

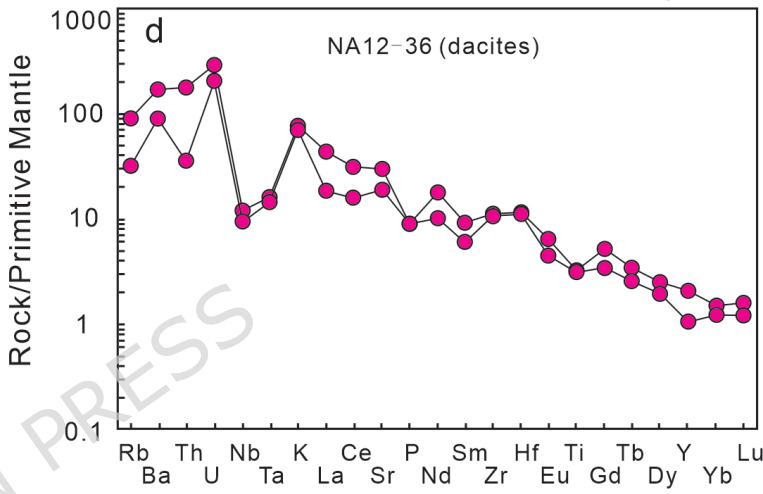

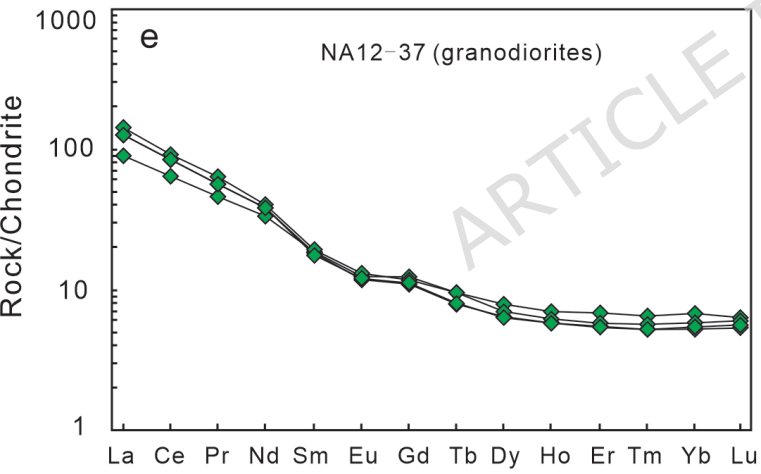

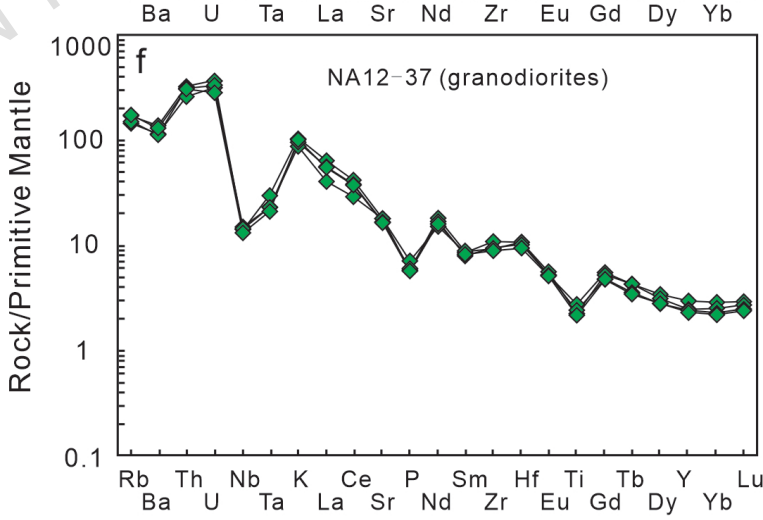

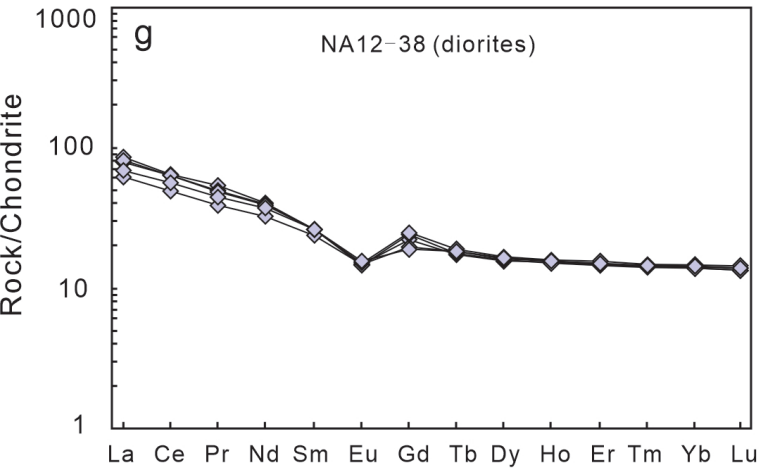

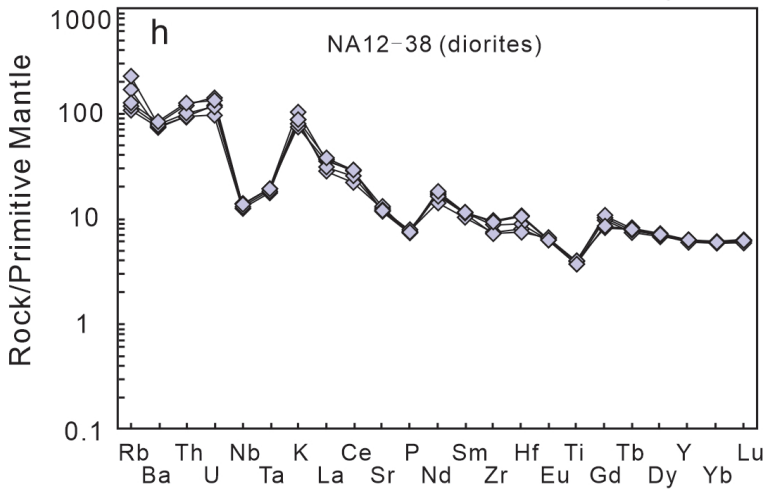

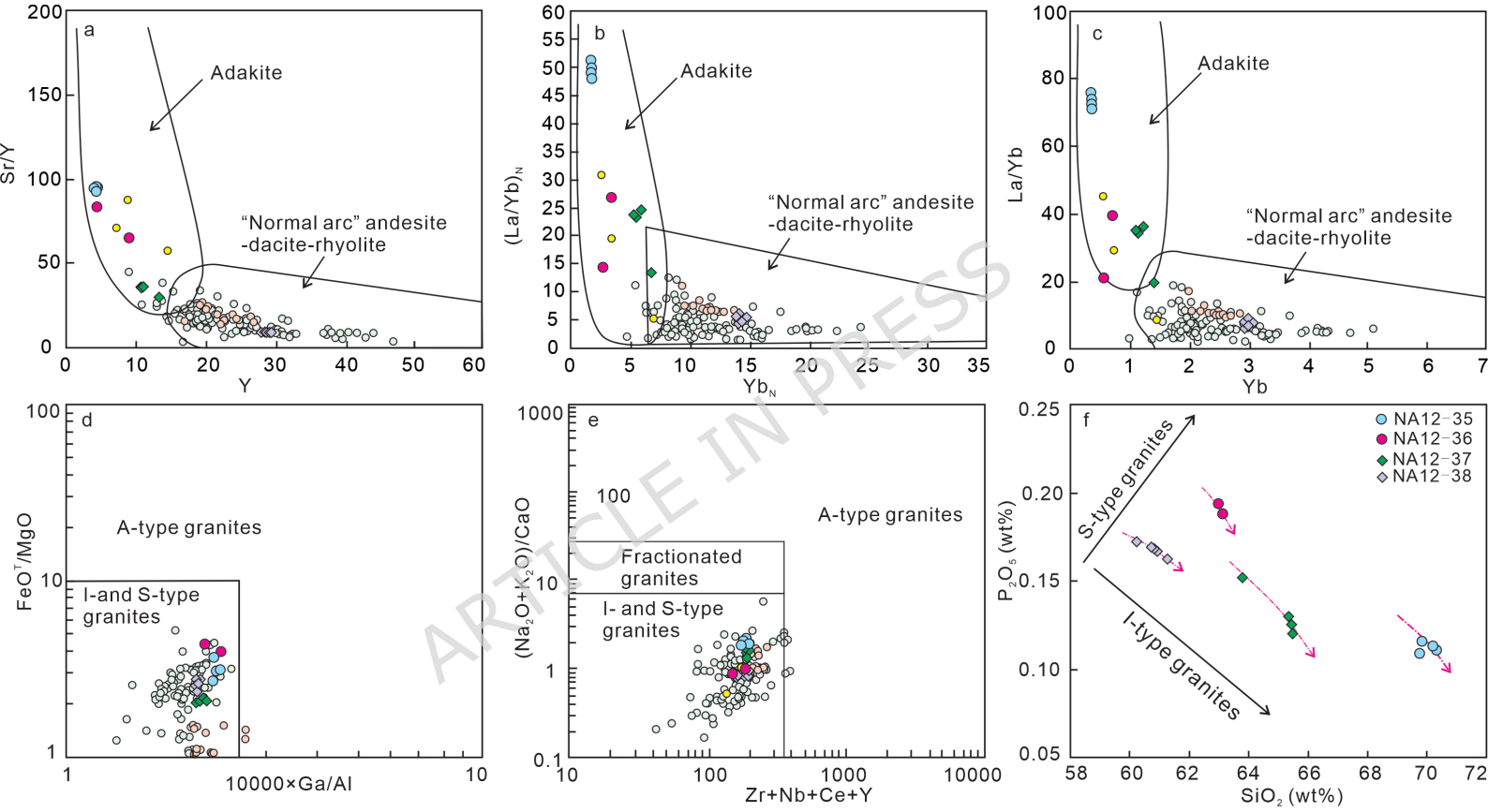

Early Miocene calc-alkaline magmatism in cental UDMA[13, 24, 28, 31, 40, 48, 50, 52]
Early Miocene adakitic rocks in cental UDMA[28-29]
Late Miocene K-rich magmatism from Ardestan and Kahang areas in the cental UDMA[24]

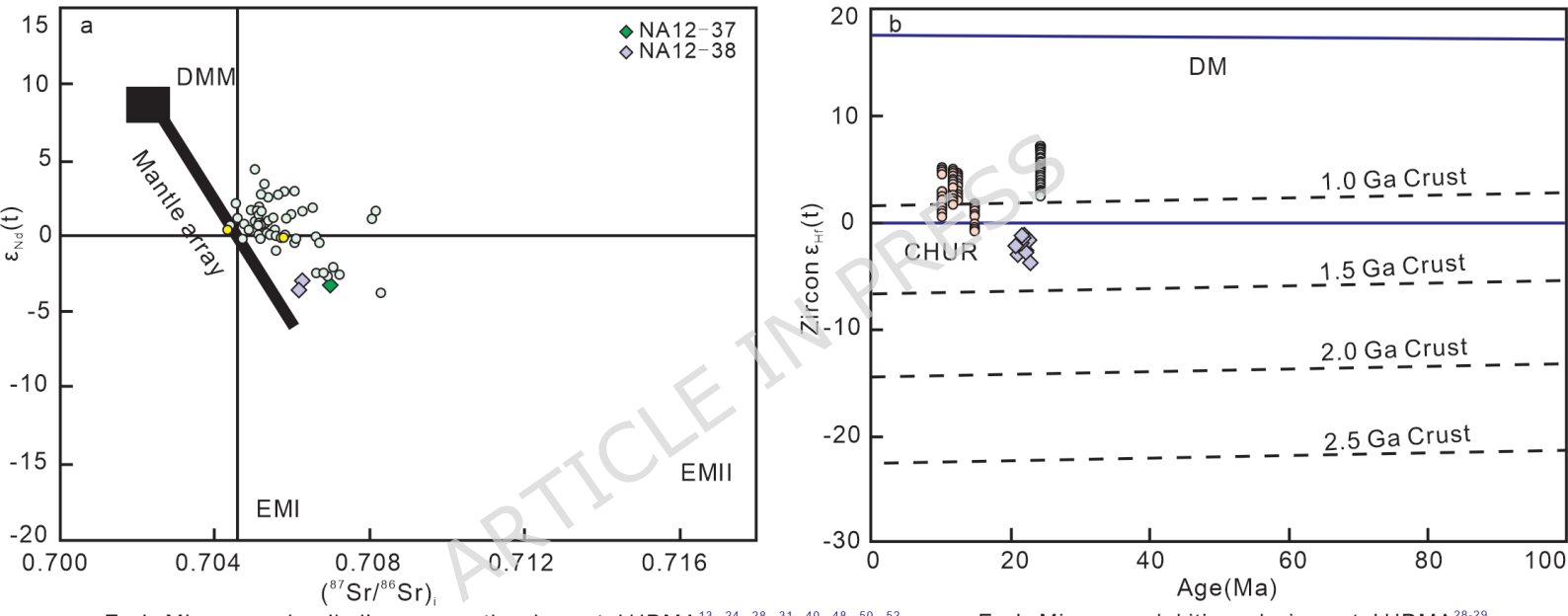

○ Early Miocene calc-alkaline magmatism in cental UDMA[13, 24, 28, 31, 40, 48, 50, 52]

○ Early Miocene adakitic rocks in cental UDMA[28-29]

○ Late Miocene K-rich magmatism from Ardestan and Kahang areas in the cental UDMA[24]

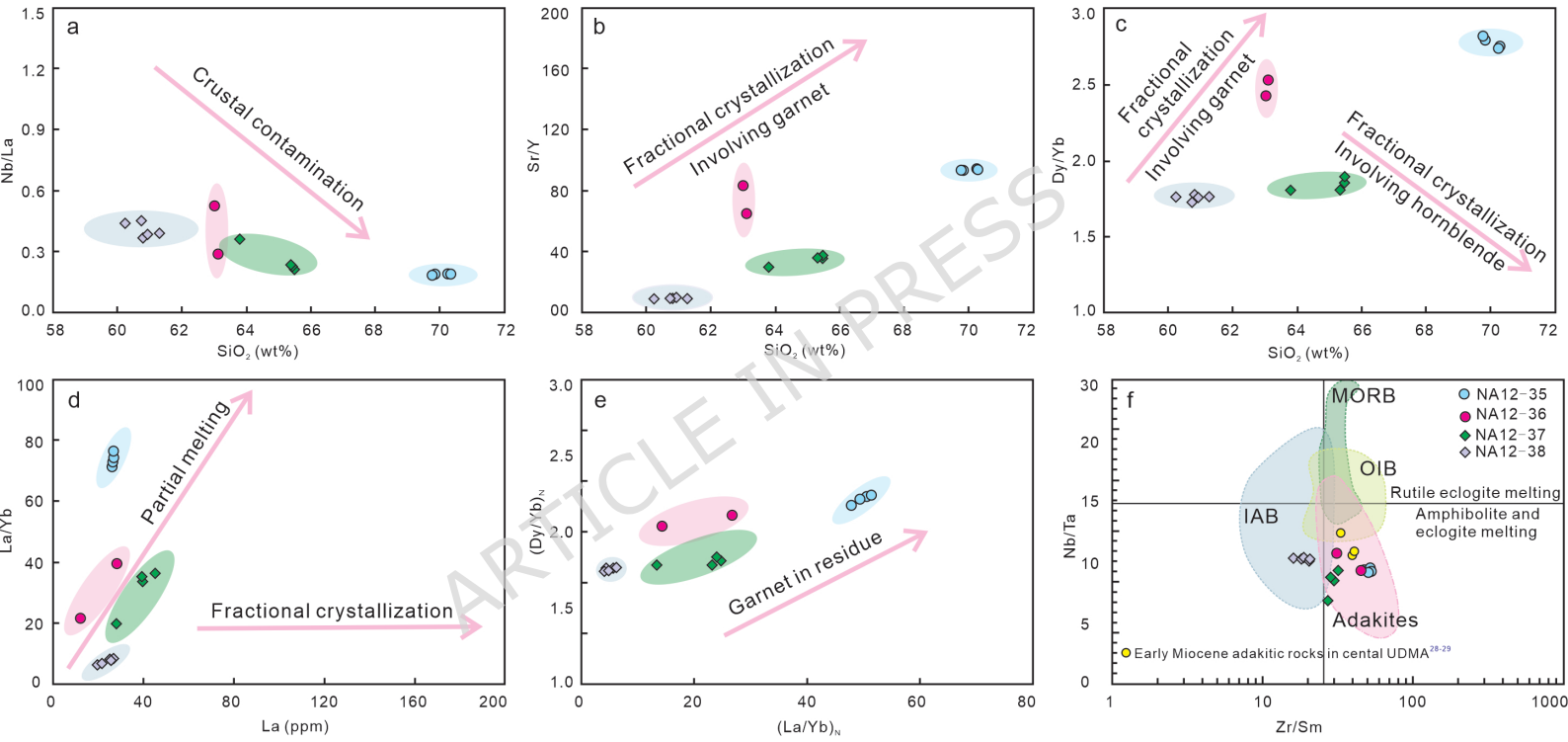

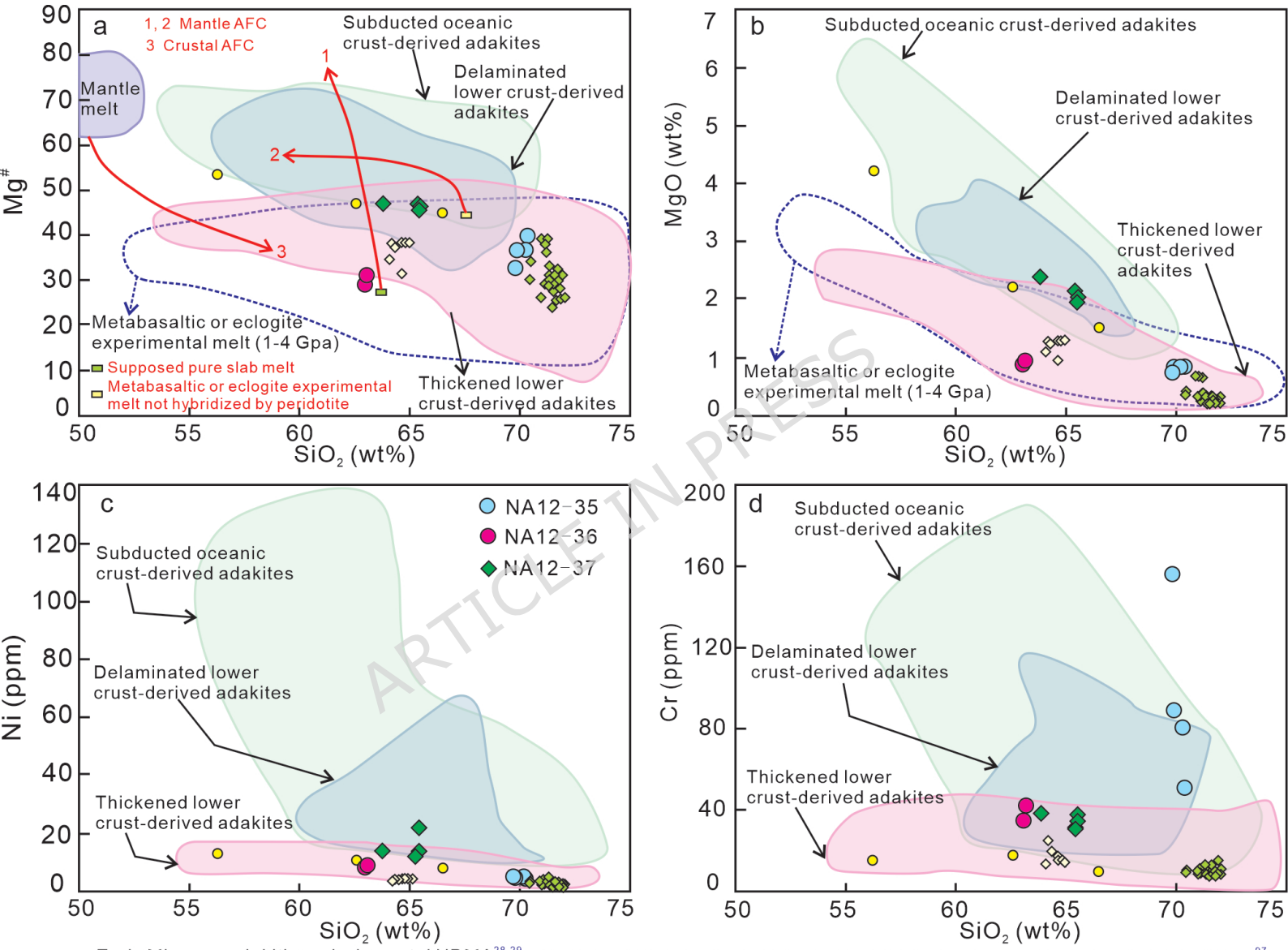

Early Miocene adakitic rocks in cental UDMA[28-29]
Adakitic magmatism by partial melting of thickened continental crust from Tibet[97]
Adakitic magmatism by partial melting of thickened continental crust from Yangtze Block[99]

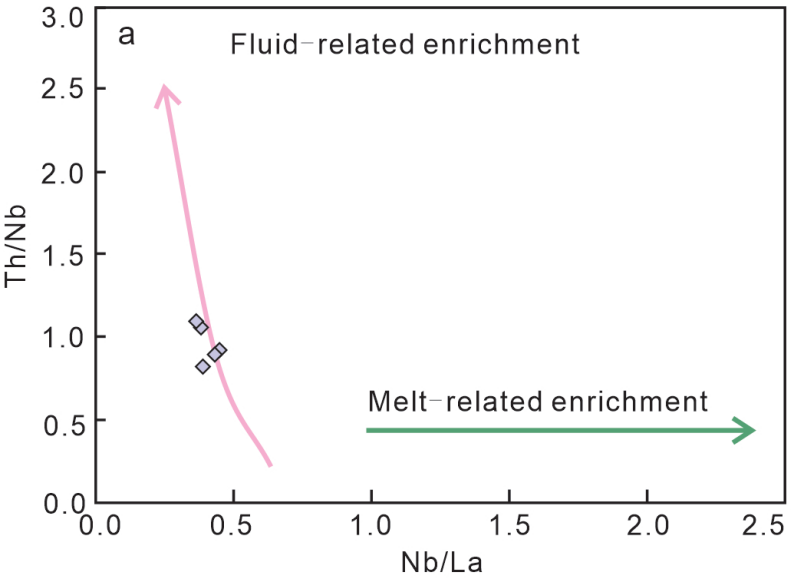

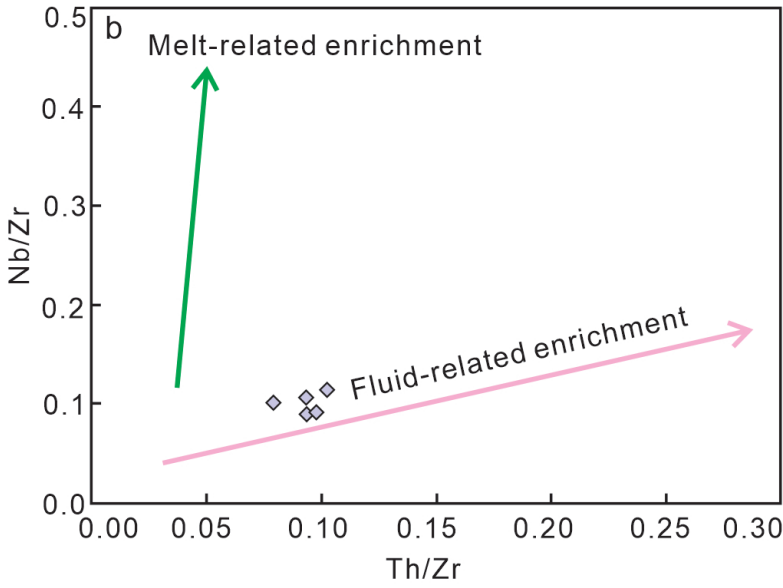

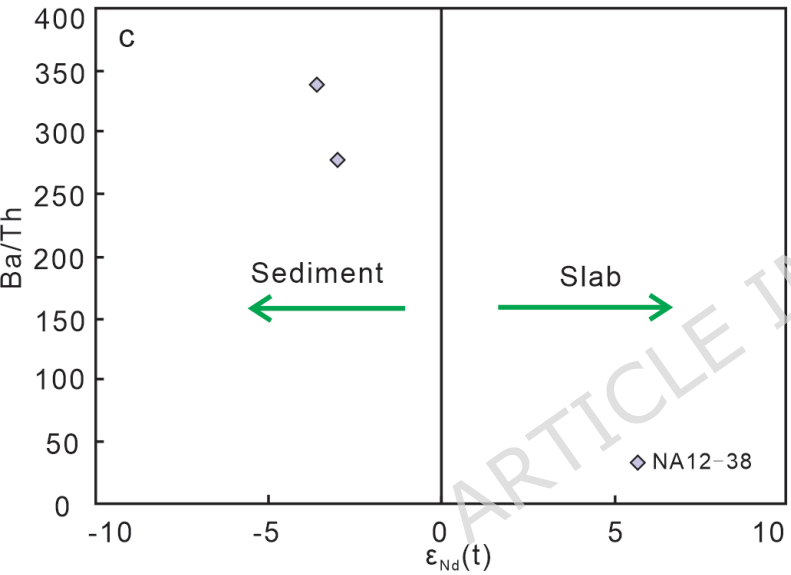

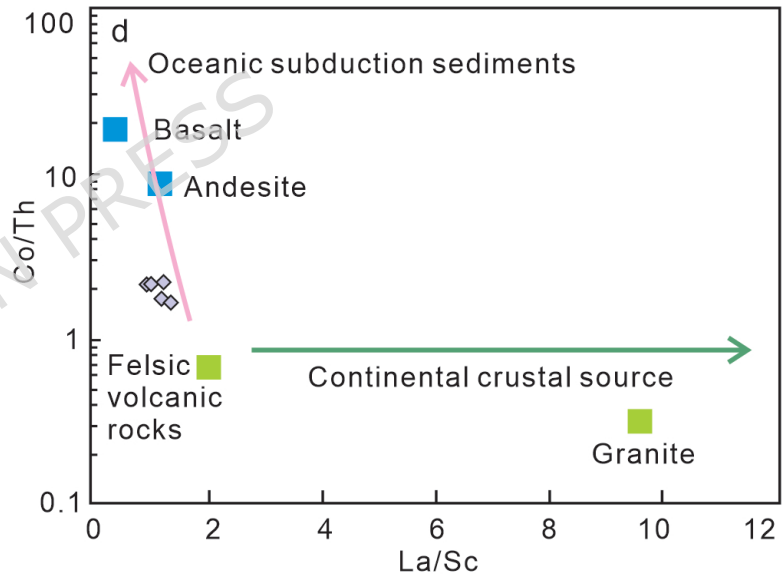

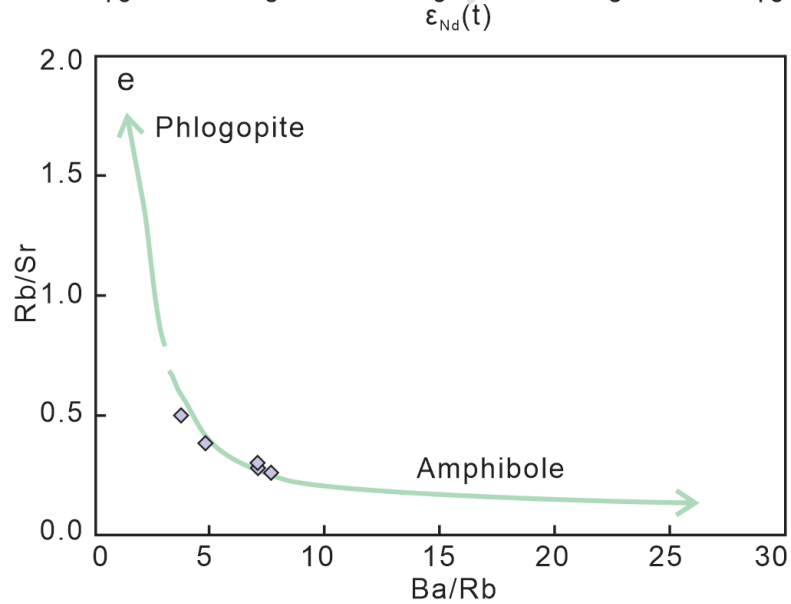

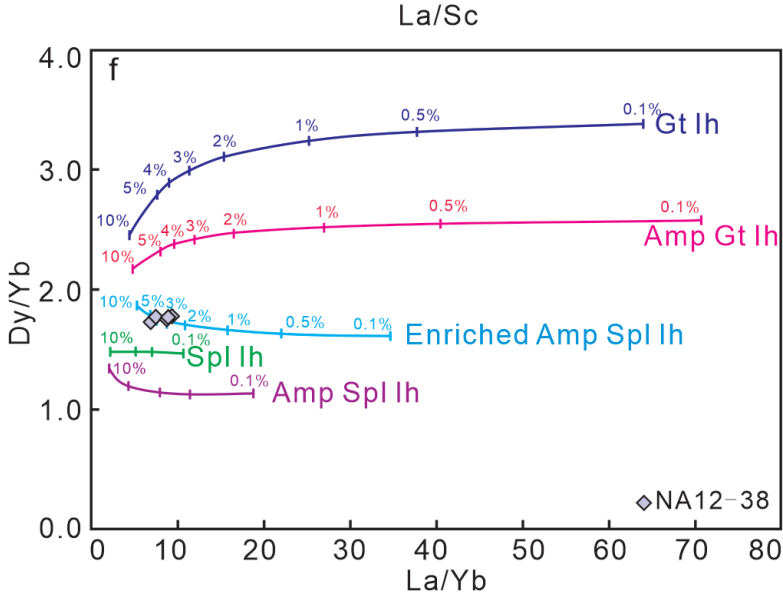

a: Oligocene (ca. ~37-25 Ma[14,16,20])

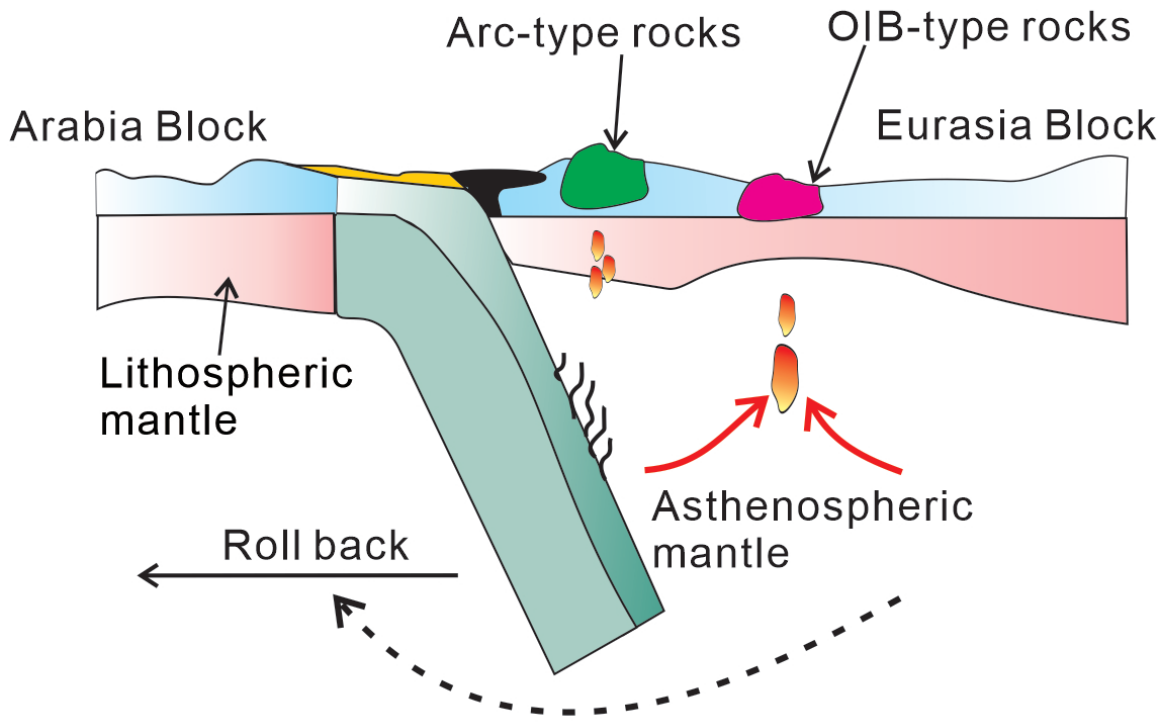

b: Early Miocene (ca. 24-22 Ma)

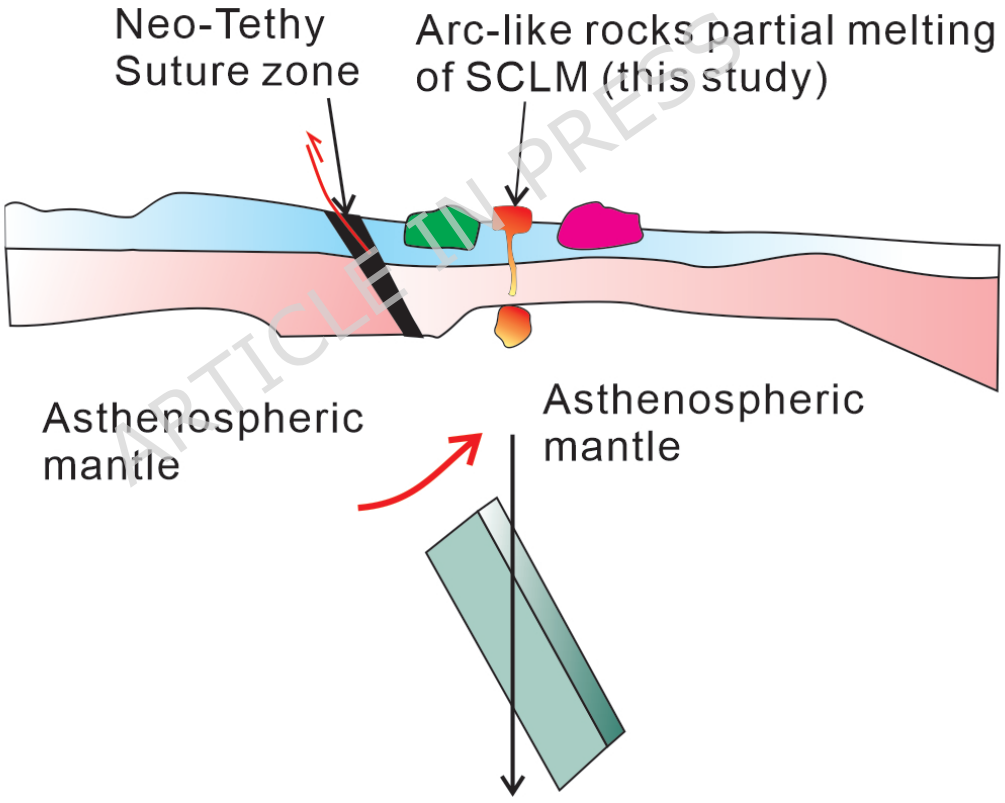

c: Early to middle Miocene (ca. 19-17 Ma)

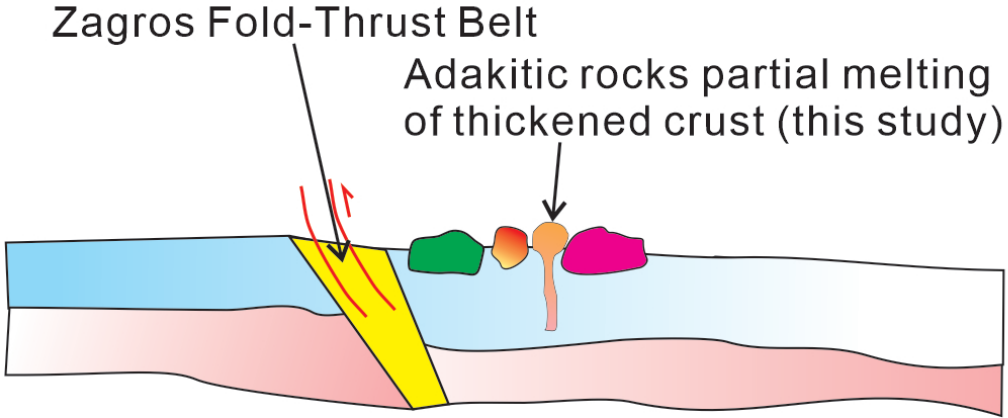

Table 1. Zircon U–Pb analytical data of diorite (NA12–38–6) in the Kashan area.

Spot	Isotopic ratio						Th/U	Age (Ma)					
	$^{207}Pb/^{206}Pb$	1σ	$^{207}Pb/^{235}U$	1σ	$^{206}Pb/^{238}U$	1σ		$^{207}Pb/^{206}Pb$	1σ	$^{207}Pb/^{235}U$	1σ	$^{206}Pb/^{238}U$	1σ
NA12-38-6-01	0.04470	0.00198	0.02095	0.00098	0.00341	0.00006	0.63	-34	56	21.1	1	21.9	0.4
NA12-38-6-02	0.04823	0.00265	0.03534	0.00204	0.00535	0.00010	0.54	111	93	35	2	34.4	0.6
NA12-38-6-03	0.04714	0.00189	0.02254	0.00100	0.00343	0.00006	0.62	56	67	22.6	1	22.1	0.4
NA12-38-6-04	0.04664	0.00154	0.02246	0.00086	0.00349	0.00006	0.70	31	53	22.6	1	22.5	0.4
NA12-38-6-05	0.04860	0.00191	0.02298	0.00099	0.00346	0.00006	0.85	129	64	23.1	1	22.3	0.4
NA12-38-6-06	0.04692	0.00195	0.02289	0.00105	0.00350	0.00006	0.86	45	63	23	1	22.5	0.4
NA12-38-6-07	0.04885	0.00220	0.02430	0.00114	0.00359	0.00007	0.61	140	67	24	1	23.1	0.5
NA12-38-6-08	0.04177	0.00236	0.02013	0.00118	0.00356	0.00008	0.52	-190	88	20	1	22.9	0.5
NA12-38-6-09	0.04957	0.00224	0.02251	0.00109	0.00332	0.00006	0.59	175	74	23	1	21.3	0.4
NA12-38-6-10	0.04701	0.00205	0.02693	0.00125	0.00417	0.00009	0.52	50	58	27	1	26.8	0.6
NA12-38-6-11	0.04619	0.00220	0.02801	0.00145	0.00468	0.00010	0.54	8	64	28	1	30.1	0.7
NA12-38-6-12	0.04680	0.00218	0.02596	0.00130	0.00414	0.00009	0.51	39	62	26	1	26.6	0.6
NA12-38-6-13	0.04916	0.00224	0.02967	0.00142	0.00454	0.00010	0.71	156	64	30	1	29.2	0.7
NA12-38-6-14	0.04604	0.00195	0.02176	0.00099	0.00339	0.00006	0.47	-	59	21.9	1	21.8	0.4
NA12-38-6-15	0.04562	0.00235	0.03324	0.00181	0.00534	0.00010	0.67	-22	73	33	2	34.3	0.7

NA12-38-6-16	0.04508	0.002116	0.02774	0.00150	0.00448	0.00010	0.57	-16	71	28	1	28.8	0.6
NA12-38-6-17	0.04621	0.00243	0.03314	0.00190	0.00533	0.00011	0.52	9	84	33	2	34.2	0.7
NA12-38-6-18	0.04353	0.00222	0.02818	0.00155	0.00479	0.00010	0.66	-95	77	28	2	30.8	0.7
NA12-38-6-19	0.04598	0.00317	0.03215	0.00273	0.00511	0.00010	0.47	-3	139	32	3	32.8	0.7
NA12-38-6-20	0.04736	0.00225	0.02953	0.00157	0.00457	0.00010	0.67	68	74	30	2	29.4	0.6
NA12-38-6-21	0.04665	0.00205	0.02048	0.00093	0.00326	0.00006	0.35	31	65	20.6	1	21	0.4

Table 2. Bulk rock composition of major (wt%) and trace elements (ppm) of samples in the Kashan area.

Sample	NA12-35-2	NA12-35-3	NA12-35-4	NA12-35-5	NA12-36-1	NA12-36-2	NA12-37-1	NA12-37-3	NA12-37-4	NA12-37-5	NA12-38-1	NA12-38-2	NA12-38-3	NA12-38-4	NA12-38-5
Rock	Rhyolite (17-19 Ma)				Dacite (17-19 Ma)		Granodiorite (17-19 Ma)				Diorite (22 Ma)				
SiO_2	70.33	69.76	70.24	69.84	63.12	63.01	63.80	65.48	65.36	65.46	60.79	61.28	60.93	60.24	60.74
TiO_2	0.32	0.34	0.34	0.32	0.67	0.66	0.57	0.49	0.51	0.46	0.82	0.87	0.86	0.87	0.83
Al_2O_3	15.43	15.33	15.49	15.35	18.13	17.65	16.19	15.76	15.81	15.77	15.46	15.55	15.53	15.48	15.56
FeO^T	2.52	3.00	2.84	2.86	4.15	4.25	5.48	4.89	4.84	4.60	8.29	7.91	7.27	8.34	7.47
MnO	0.08	0.14	0.11	0.11	0.05	0.07	0.09	0.09	0.08	0.08	0.18	0.17	0.15	0.16	0.14
MgO	0.84	0.74	0.83	0.84	0.94	0.88	2.45	2.06	2.16	1.99	3.03	3.10	3.08	3.03	3.13
CaO	3.36	3.69	3.17	3.62	6.46	7.05	4.81	4.26	4.37	4.18	6.01	5.94	6.11	6.36	6.59
Na_2O	4.38	4.34	4.27	4.38	4.08	4.12	3.80	3.68	3.81	4.18	2.65	2.69	2.75	2.90	2.67
K_2O	2.63	2.55	2.60	2.57	2.21	2.12	2.65	3.17	2.95	3.15	2.61	2.33	3.14	2.45	2.69
P_2O_5	0.11	0.11	0.11	0.12	0.19	0.19	0.15	0.12	0.13	0.12	0.17	0.16	0.17	0.17	0.17
LOI	1.55	1.11	1.26	1.59	2.64	2.39	0.61	0.85	0.86	0.72	1.09	1.64	1.24	1.34	1.14
$Mg^{\#}$	39.8	32.7	36.7	36.6	31.1	29.0	47.0	45.5	46.9	46.2	42.0	43.7	45.6	41.9	45.3
La	25.89	26.51	26.04	26.70	28.27	12.08	28.29	45.18	39.65	39.31	26.45	24.74	25.34	21.29	19.31
Ce	45.02	45.63	45.16	46.17	52.38	26.96	52.39	76.03	68.90	68.07	52.40	51.97	50.73	45.28	39.34
Pr	4.76	4.75	4.78	4.83	6.06	3.36	5.67	7.93	7.01	6.88	6.53	6.09	5.89	5.42	4.71
Nd	16.35	16.42	16.64	16.78	22.71	13.29	20.28	24.80	23.29	23.13	24.14	24.06	23.16	22.08	19.37
Sm	2.52	2.54	2.57	2.61	3.85	2.52	3.69	3.83	3.52	3.66	5.17	5.18	5.18	5.06	4.63
Eu	0.67	0.69	0.68	0.68	1.04	0.71	0.92	0.98	0.89	0.89	1.09	1.08	1.10	1.13	1.07
Gd	1.90	1.96	1.95	2.00	2.91	1.97	3.24	3.08	2.91	2.90	5.07	6.22	6.45	4.90	5.76
Tb	0.21	0.21	0.21	0.21	0.36	0.26	0.46	0.46	0.39	0.38	0.87	0.85	0.89	0.87	0.82
Dy	0.98	0.99	1.00	1.00	1.80	1.37	2.55	2.30	2.07	2.10	5.24	5.17	5.42	5.32	5.08
Ho	0.16	0.17	0.17	0.17	0.32	0.25	0.51	0.46	0.42	0.42	1.12	1.10	1.16	1.14	1.11
Er	0.41	0.41	0.42	0.42	0.81	0.64	1.46	1.23	1.14	1.16	3.09	3.08	3.27	3.18	3.09
Tm	0.06	0.06	0.06	0.06	0.11	0.09	0.21	0.19	0.17	0.17	0.47	0.46	0.48	0.47	0.46
Yb	0.36	0.35	0.37	0.36	0.71	0.57	1.42	1.24	1.15	1.11	2.95	2.94	3.09	3.01	2.95
Lu	0.05	0.05	0.06	0.06	0.11	0.09	0.21	0.20	0.19	0.18	0.46	0.45	0.48	0.46	0.45
Y	4.38	4.36	4.42	4.47	9.15	4.52	13.48	11.17	10.92	10.85	28.72	28.21	29.17	29.33	28.87
Sc	3.47	3.53	3.79	3.99	9.50	4.99	10.48	7.39	8.46	8.20	20.09	20.77	22.01	21.96	21.69
V	25.07	27.48	26.03	25.94	97.22	96.80	95.65	82.08	75.17	82.30	165.10	156.10	162.30	171.80	169.10
Cr	50.55	156.10	80.71	88.87	41.89	34.38	38.05	36.70	30.27	34.10	15.24	19.72	28.25	13.64	14.29
Co	4.02	4.41	4.28	4.56	12.62	9.43	11.99	10.76	11.48	11.67	17.18	16.97	17.53	17.77	16.59
Ni	4.56	5.32	5.30	4.89	9.25	8.50	14.19	22.13	12.64	14.08	6.49	6.87	15.75	5.95	6.12
Cu	15.23	18.13	22.65	18.10	30.37	30.22	64.66	29.09	140.10	12.28	24.33	22.56	18.54	27.55	15.85
Pb	26.43	15.83	15.96	16.60	22.73	15.00	25.06	24.45	16.40	28.21	16.64	24.51	13.29	17.26	50.56
Ga	18.09	18.03	18.46	18.64	21.89	19.52	17.92	17.52	16.96	17.94	16.64	16.55	16.68	16.99	16.84
Rb	75.34	75.19	76.88	78.06	54.18	19.07	92.79	107.30	98.28	111.50	81.19	67.71	146.60	75.85	105.50

Sr	409.2	408.9	416.7	416.7	595.4	377.2	403.4	409.0	391.7	390.4	268.5	258.0	289.5	265.1	271.3
Zr	129.7	120.8	136.3	137.9	120.1	114.1	117.7	102.5	105.5	101.0	106.4	97.5	107.6	81.3	84.0
Nb	4.84	4.86	4.90	4.97	8.08	6.33	10.07	9.28	9.25	8.81	9.66	9.61	9.68	9.31	8.67
Cs	2.65	2.75	2.26	2.71	3.43	4.04	3.65	3.80	2.32	4.19	2.59	1.80	3.63	1.55	3.92
Ba	867.9	861.3	877.2	868.9	1121.7	617.8	786.8	957.3	778.1	897.2	579.6	525.9	553.1	545.5	510.5
Hf	3.55	3.39	3.70	3.67	3.36	3.23	3.37	3.27	3.15	2.92	3.31	2.81	3.35	2.36	2.52
Ta	0.44	0.44	0.45	0.44	0.63	0.57	0.91	1.15	0.92	0.83	0.80	0.78	0.80	0.76	0.71
Th	9.52	9.55	9.77	9.67	14.21	2.66	20.95	26.85	25.27	24.76	10.48	7.79	10.15	8.38	7.90
U	2.72	4.32	2.87	2.89	5.66	4.17	6.59	7.42	6.69	6.18	2.77	2.52	2.99	2.40	2.05
Ti	1859	1863	1909	1929	4129	3737	3541	3122	3139	3271	5116	5014	5096	5172	4920
Mn	576.5	964.6	746.8	873.3	423.4	464.1	683.2	697.6	612.2	680.7	1394.1	1286.7	1154.5	1254.6	1079.5
Zn	40.59	30.68	38.42	40.58	168.20	75.59	52.06	48.04	42.83	57.20	77.81	77.30	86.70	93.72	96.43
Ge	0.74	0.81	0.80	0.89	1.54	0.88	1.51	1.29	1.33	1.42	1.73	1.68	1.64	1.67	1.57

$Mg^{\#}$ = 100 × Mg/[Mg + Fe^{2+}]; FeO^{T} = Total FeO; FeO = 0.8998 × FeO^{T}. The major elements shown in the table were normalized to 100% anhydrous.

Table 3. Sr–Nd isotopic compositions of samples in the Kashan area.

Sample	Rock	$^{87}Rb/^{86}Sr$	$^{87}Sr/^{86}Sr$	$^{147}Sm/^{144}Nd$	$^{143}Nd/^{144}Nd$	T (Ma)	$(^{87}Sr/^{86}Sr)_i$	$(^{143}Nd/^{144}Nd)_i$	εNd(t)	T_{DM} (Ma)	T_{2DM} (Ma)
NA12-37-3	Granodiorite	0.7693	0.707179	0.0940	0.512458	17	0.706997	0.511448	−3.3	882	1103
NA12-38-1	Diorite	0.8868	0.706546	0.1301	0.512475	22	0.706269	0.512456	−3.0	1233	1080
NA12-38-2	Diorite	0.7696	0.706421	0.1309	0.512446	22	0.706181	0.512427	−3.6	1298	1126

Table 4. Lu–Hf isotopic compositions of diorite (NA12–38–6) in the Kashan area.

Spots	Age (Ma)	$^{176}Yb/^{177}Hf$	$^{176}Lu/^{177}Hf$	2σ	$^{176}Hf/^{177}Hf$	2σ	$^{176}Hf/^{177}Hf_{(i)}$	$\varepsilon_{Hf}(0)$	$\varepsilon_{Hf}(t)$	T_{DM}	T_{DM}^{C}	$f_{Lu/Hf}$
NA12-38-6-01	21.9	0.057227	0.001797	0.000002	0.282732	0.000015	0.282732	−1.4	−0.9	753	1161	-0.95
NA12-38-6-03	21.1	0.052664	0.001684	0.000004	0.282726	0.000015	0.282726	−1.6	−1.2	759	1175	-0.95
NA12-38-6-04	22.5	0.032715	0.001054	0.000008	0.282693	0.000015	0.282693	−2.8	−2.3	793	1248	-0.97
NA12-38-6-05	22.3	0.064289	0.002081	0.000005	0.282734	0.000016	0.282733	−1.3	−0.9	756	1158	-0.94
NA12-38-6-06	22.5	0.041515	0.001364	0.000015	0.282688	0.000016	0.282687	−3.0	−2.5	808	1261	-0.96
NA12-38-6-07	23.1	0.052402	0.001682	0.000012	0.282661	0.000016	0.282660	−3.9	−3.5	854	1322	-0.95
NA12-38-6-08	22.9	0.043632	0.001428	0.000034	0.282721	0.000018	0.282720	−1.8	−1.4	762	1188	-0.96
NA12-38-6-09	21.3	0.045408	0.001462	0.000002	0.282683	0.000016	0.282682	−3.2	−2.7	816	1272	-0.96
NA12-38-6-14	21.8	0.060026	0.001922	0.000011	0.282713	0.000018	0.282712	−2.1	−1.6	784	1206	-0.94
NA12-38-6-21	21.0	0.032987	0.001051	0.000002	0.282706	0.000014	0.282705	−2.4	−1.9	776	1221	-0.97